Journal of Computational Physics 230 (2011) 5974–5995

Contents lists available at ScienceDirect

Journal of Computational Physics

journal homepage: www.elsevier.com/locate/jcp

# Artificial boundary conditions for the numerical solution of the Euler equations by the discontinuous galerkin method

Ioannis Toulopoulos [a,b,*], John A. Ekaterinaris [b,c]

[a] Institute of Applied Mathematics, University of Freiburg, Germany
[b] FORTH/IACM, Heraklion, Crete, Greece
[c] Department of Mechanical and Aerospace Engineering, University of Patras, Greece

ARTICLE INFO

*Article history:*
Received 22 December 2009
Received in revised form 4 April 2011
Accepted 6 April 2011
Available online 16 April 2011

*Keywords:*
Euler's equations
Artificial boundary conditions
Characteristic analysis
High-order discontinuous Galerkin methods

ABSTRACT

We present artificial boundary conditions for the numerical simulation of compressible flows using high-order accurate discretizations with the discontinuous Galerkin (DG) finite element method. The construction of the proposed boundary conditions is based on characteristic analysis and applied for boundaries with arbitrary shape and orientation. Numerical experiments demonstrate that the proposed boundary treatment enables to convect out of the computational domain complex flow features with little distortion. In addition, it is shown that small-amplitude acoustic disturbances could be convected out of the computational domain, with no significant deterioration of the overall accuracy of the method. Furthermore, it was found that application of the proposed boundary treatment for viscous flow over a cylinder yields superior performance compared to simple extrapolation methods.

© 2011 Elsevier Inc. All rights reserved.

## 1. Introduction

Simulation of realistic flows requires truncation of the computational domain in order to minimize computational effort and discretize the region of interest with sufficiently fine resolution. Therefore, artificial boundaries, which must enclose the region of interest, are introduced. On these boundaries, artificial boundary conditions (ABCs) that do not damage the solution must be imposed. This task is relatively easier when the flow near the boundary can be linearized and analytical solutions in the truncated part of the domain may be used to derive ABCs. In this case, artificial (numerical) boundary conditions are obtained on boundaries by requiring that there are no incoming waves [1,2]. However, when the flow at the artificial boundary cannot be linearized about a uniform state, development of truly nonreflective boundary conditions is not possible. For these cases, ABCs must be combined with sponge regions [3–5], which are added as an ad hoc boundary treatment that absorbs reflections and minimizes numerical perturbations created at the artificial boundaries.

The increase of computing power has made possible the use of high order methods [6,7], for numerical simulation of transition and turbulence. The ability of such methods to retain their theoretical order of accuracy is determined by boundary conditions which have to be included in the numerical scheme [8]. It has long being recognized that accurate simulation of compressible flows requires control of wave reflections from the boundaries of the computational domain [1]. The boundary treatment problem is simpler for steady-state numerical simulations because evolution of the waves at the boundary is of no interest and therefore these waves can be eliminated. The mechanism by which these waves (especially acoustic

* Corresponding author at: Institute of Applied Mathematics, University of Freiburg, Germany.
*E-mail addresses:* toulioa@iacm.forth.gr, ioannis.toulopoulos@math.uni-freiburg.de (I. Toulopoulos), ekaterin@iacm.forth.gr (J.A. Ekaterinaris).

0021-9991/$ - see front matter © 2011 Elsevier Inc. All rights reserved.
doi:10.1016/j.jcp.2011.04.008

disturbances) are eliminated is often numerical dissipation of the numerical scheme, and/or grid stretching or sponge regions. An improvement over sponge regions is the recently developed PML approach for the Navier–Stokes equations [9]. High order accurate methods, however, minimize numerical viscosity. Therefore in high resolution time dependent simulations acoustic waves and other physical or numerical waves have to be eliminated by other mechanisms such as nonreflective or absorbing boundary conditions [3,7,10].

Purely nonreflective boundary conditions based on linearization near the boundary are appropriate for inflow and radiation problems. Several techniques were developed for radiation boundary treatment [11–14]. These techniques were tested by Hixon et al. [15], for aeroacoustic propagation. It was found [13], that linearized radiation ABC's usually provide sufficient accuracy at the outflow boundary for aeroacoustics. For the nonlinear case, improved accuracy at these boundaries can be achieved by combining ABCs with sacrificial regions, where the governing equations are modified in a finite region adjacent to the boundary [3–5]. In [4,5], this type of boundary conditions based on grid stretching and damping have been presented for the nonlinear and linear case, respectively. The parts of the computational domain, where a modified set of equations is used, are known as sponge or buffer zones, fridge regions or absorbing layers, and can be used in combination with nonreflective boundary conditions. Recently, Zhou and Wang [16], used absorbing sponge zones with the high order spectral difference method. An effective technique to specify boundary conditions for hyperbolic problems is to use characteristic theory that specifies the different waves crossing a boundary. This method has been extensively studied and successfully applied by Thompson [11,17], Poinsot and Lele [18], Sele et al. [19] and Colonious et al. [2,20,21], for finite difference numerical simulations. Implementation of the boundary conditions of Poinsot and Lele in the finite volume context [22], for second-order accurate schemes is straightforward. On the other hand, implementation of these boundary conditions for high order discontinuous Galerkin finite element discretizations (DGFE), where boundary data outside of the computational domain are required to complete the scheme, has not been demonstrated.

The objective of this paper is to use the characteristic analysis of the Euler equations and develop a methodology for the construction of artificial (numerical) boundary conditions in the DGFE context. In order to build up our methodology and incorporate the proposed boundary treatment in the DGFE framework, we use the *mirror* (*ghost*) *element* technique and specify the required data at the edges of these elements through characteristic analysis. The proposed method does not require a-priori knowledge of the behavior of the solution outside of the domain, in order to estimate the characteristic waves crossing the outflow boundary (for example in [18] a methodology to express the incoming waves in relation to outgoing waves is presented). All the waves are estimated in the mirror element. Applying the characteristic analysis in the mirror element, we derive a system of ordinary differential equations (ODE system). This system relates the time variations of the state variables to the variations of the characteristic waves. This system of ODE's defines the characteristic based BCs, hereafter denoted as CHBC–ODE. The right hand side of CHBC–ODE is computed using the boundary solution data from the previous time step and avoids specification of the waves using information from the exterior of the domain.

Numerical experiments demonstrate that use of these artificial boundary conditions with DG discretizations makes possible the convection of vortical disturbances away from the computational domain with little distortion. The proposed boundary treatment was further applied for viscous flow and aeroacoustic problems. For the latter case, the full nonlinear-Euler equations are used and aeroacoustic disturbances are specified as small perturbations in pressure.

The rest of this paper is organized as follows. In Section 2, we present the formulation of the discontinuous Galerkin method for the Euler equations. Section 3 presents the characteristic analysis and describes in detail the proposed characteristic based BC's for arbitrary shape boundaries. The approximation of the characteristic waves on the local polynomial space of the mirror elements, the expression of CHBC–ODE system and the estimation of the values of the state vector in the mirror elements, are also included in this section. In Section 4, the accuracy of DGFE discretizations utilizing the proposed ABC's is evaluated with numerical examples for inviscid and viscous flow and for linear (aeroacoustic-like) disturbances impinging on the artificial boundaries. In all cases, high order of accuracy at the artificial boundary is achieved. Finally, in the appendix the CHBC form for the linearized Euler equations is analyzed.

## 2. Governing equations and space discretization

The equations governing two-dimensional, inviscid, compressible flow are the Euler equations. The conservative form of these equations is

$$\partial_t \mathbf{u} + \partial_x \mathbf{f}(\mathbf{u}) + \partial_y \mathbf{g}(\mathbf{u}) = 0, \quad \text{in} \quad \Omega \times (0, T), \tag{2.1}$$

where $T > 0$ is the length of the time interval and $\Omega$ is a bounded domain of $\mathbb{R}^2$. In (2.1) the conservative variable vector and the Cartesian flux vectors are given by

$$\mathbf{u} = \begin{bmatrix} \rho \\ \rho u \\ \rho v \\ \rho e \end{bmatrix}, \quad \mathbf{f}(\mathbf{u}) = \begin{bmatrix} \rho u \\ \rho u^2 + p \\ \rho u v \\ (\rho e + p) u \end{bmatrix}, \quad \mathbf{g}(\mathbf{u}) = \begin{bmatrix} \rho v \\ \rho u v \\ \rho v^2 + p \\ (\rho e + p) v \end{bmatrix}. \tag{2.2}$$

Here, $p$ is the pressure, $\rho e$ is the total energy, and $\mathbf{v} = (u, v)$ is the velocity. The system is completed by the equation of state for a perfect gas,

$$p = (\gamma - 1)\left[\rho e - \rho\frac{1}{2}(u^2 + v^2)\right], \tag{2.3}$$

where $\gamma = 1.4$ is the ratio of the specific heats. For the system (2.1), we consider an initial condition

$$\mathbf{u}(x, y, 0) = \mathbf{u}_0(x, y), \tag{2.4}$$

where $\mathbf{u}_0(x,y)$ is a given function, and the boundary conditions that we present and apply in the numerical examples have the form

$$\mathbf{B}(\mathbf{u}_t(x, y, t)) = 0, \quad \text{on} \quad \partial\Omega \times (0, T), \tag{2.5}$$

where $\mathbf{B}$ will be specified in Section 3.

### 2.1. The discontinuous Galerkin space discretization

Let $T_h$ be a triangulation of the domain $\Omega$ consisting of a collection of non-overlapping triangular elements $\bigcup_{el=1}^{Nel} E_{el}$, thus $T_h = \bigcup_{el=1}^{Nel} E_{el} = \Omega$. For every element $E \in T_h$ we define a local polynomial space $V_h(E)$ of dimension $k$ whose basis functions $P_j$ are polynomials of degree at most $m$, i.e. $V_h(E) = \mathbb{P}^m(E)$ and $P_j,\ j = 1, \ldots, k \in \mathbb{P}^m(E)$. The dimension $k$ of the space $V_h(E)$ is given by the formula $k = \frac{(2+m)!}{2!m!}$. In our numerical examples up to third order polynomials are used. The approximate solution $\mathbf{u_h}$ is sought in the *discontinuous* finite element space $\mathbf{V}_h$

$$\mathbf{V}_h = \{v \in L^2(\Omega) : v|_E \in V_h(E)\ \forall\ E \in T_h\}.$$

For each element $E \in T_h$, the components $u_h^i,\ i = 1, 2, 3, 4$ of the approximate conservative variable vector $\mathbf{u}_h$ have the representation

$$u_h^i = \sum_{j=1}^{k} c(t)_j^i P_j(x, y), \quad i = 1, 2, 3, 4, \tag{2.6}$$

where $c(t)_j^i$ are the degrees of freedom to be advanced in time. For every $E \in T_h$, we write the degrees of freedom of the components of $\mathbf{u}_h$, as a vector denoted by $\mathbf{U}$. The finite element space does not require any continuity across inter-element boundaries.

#### 2.1.1. Basis functions

The space $V_h(E)$ is spanned by the nodal Lagrange polynomial basis functions $P_j$, $j = 1,\ldots,k$, which are not orthogonal. For every element each polynomial $P_j$ of the base is equal to one at the node $N_j$ and zero at the other nodes. In addition, the support of a polynomial basis $P_j \in V_h(E_m)$ on $\partial E$ consists of the edges which include the node $N_j$. More details about the basis functions can be found in [23].

### 2.2. The space-discrete weak formulation

Let $E \in T_h$, and $\mathbf{u}_h \in V_h(E)$ be the approximation of $\mathbf{u}$. In order to determine the approximate solution of (2.1) in $V_h(E)$ we consider the weak form of (2.1)

$$\int_E \partial_t \mathbf{u}\, v - \int_E (\mathbf{f}(\mathbf{u}), \mathbf{g}(\mathbf{u})) \cdot \nabla v\, dx\, dy + \int_{\partial E} (\mathbf{f}(\mathbf{u}), \mathbf{g}(\mathbf{u})) \cdot \mathbf{n}\, v\, ds = 0 \tag{2.7}$$

for any smooth function $v$. Replace $\mathbf{u}$ by $\mathbf{u}_h$,$v$ by a test function $\varphi$ that belongs to the finite element space $V_h$, and obtain

$$\int_E \partial_t \mathbf{u}_h \varphi - \int_E (\mathbf{f}(\mathbf{u}_h), \mathbf{g}(\mathbf{u}_h)) \cdot \nabla \varphi\, dx\, dy + \int_{\partial E} (\mathbf{f}(\mathbf{u}_h), \mathbf{g}(\mathbf{u}_h)) \cdot \mathbf{n} \varphi\, ds = 0, \quad \forall \quad \varphi \in V_h(E). \tag{2.8}$$

Here $\mathbf{n}$ denotes the outward unit normal to the boundary $\partial E$ of $E$. The line integral in (2.8) is not well defined since the finite element space $V_h(E)$ does not require continuity of the approximate solution at the interfaces. Therefore, following the finite volume approach, we replace the flux $(\mathbf{f},\mathbf{g})\cdot\mathbf{n}$ by a numerical flux function $h$, which depends on the two values of $\mathbf{u}_h$ at the interface of the element. One is the value obtained from the interior of the element $E$, denoted as $\mathbf{u}_h|_E$, and the other is the value obtained from the adjacent element $E_{adj}$ sharing common edge with $E$ and is denoted as $\mathbf{u}_h|_{E_{adj}}$,

$$h = h(\mathbf{u}_h|_E, \mathbf{u}_h|_{E_{adj}}, \mathbf{n}).$$

For simplicity, hereafter we denote $\mathbf{u_h}|_E$ as $\mathbf{u_h^{in}}$ and $\mathbf{u_h}|_{E_{adj}}$ as $\mathbf{u_h^{out}}$. Any consistent approximate Riemann solver can be used to evaluate the numerical flux [24]. In our numerical implementation, the Lax–Friedrich's (LF) numerical flux is used. The line integral in (2.8) with the LF flux takes the form,

$$\int_{\partial E} h(\mathbf{u}_h^{in}, \mathbf{u}_h^{out}, \mathbf{n}) \varphi ds = \frac{1}{2} \int_{\partial E} \left( (\mathbf{f}^{in} + \mathbf{f}^{out}, \mathbf{g}^{in} + \mathbf{g}^{out}) \cdot \mathbf{n} - \lambda\left(\mathbf{u}_h^{out} - \mathbf{u}_h^{in}\right)\right) \varphi\, ds, \tag{2.9}$$

$$\lambda = \max_{(x,y)\in\partial E} \{|\lambda_i(x, y)|\}, \quad i = 1, 2, 3, 4,$$

where $\lambda_i$ are the eigenvalues of the flux Jacobian $\mathbf{J} = \frac{\partial(\mathbf{f},\mathbf{g})\cdot\mathbf{n}}{\partial\mathbf{u}}$. With these notations, the discrete problem can be expressed as: for every $E \in T_h$ find $\mathbf{u}_h \in V_h(E)$ such that

$$\int_E \partial_t \mathbf{u}_h \varphi \, dx\, dy - \int_E (\mathbf{f}(\mathbf{u}_h), \mathbf{g}(\mathbf{u}_h)) \cdot \nabla\varphi \, dx\, dy + \int_{\partial E} h(\mathbf{u}_h^{in}, \mathbf{u}_h^{out}, \mathbf{n}) \varphi \, ds = 0, \quad \forall \varphi \in V_h(E). \tag{2.10}$$

Clearly, for elements on the boundary of the computational domain appropriate values of the state variables vector $\mathbf{u}_h^{out}$ must be determined. The subject of this paper is application of a procedure for appropriate specification of the state vector values for the mirror elements on the boundary so that reflected waves are minimized, stability is retained, and the overall accuracy of the method does not deteriorate.

### 2.3. Temporal discretization

Replacing $\varphi$ in Eq. (2.10) by the polynomial basis functions $P_j$, a system of ordinary differential equation (ODE) is obtained for the degrees of freedom $\mathbf{U}$,

$$M\frac{d\mathbf{U}}{dt} = L(\mathbf{U}), \tag{2.11}$$

where $M$ is the mass matrix. This ODE system may be advanced in time by implicit or explicit schemes. Here we use the explicit third order TVD Runge–Kutta method introduced in [25]. Let $\{t^n\}_{n=1}^{N-1}$ be a uniform partition of the time interval $[0,T]$. Set $\Delta t = t^{n+1} - t^n$, $n = 0, 1, 2, \ldots, N-1$ where $N\Delta t = T$. The three intermediate stages of one Runge–Kutta cycle, from $t^n$ to $t^{n+1}$ are

$$\begin{aligned}
\mathbf{U}^{n,1} &= \mathbf{U}^n + \Delta t M^{-1} L(\mathbf{U}^n),\\
\mathbf{U}^{n,2} &= \frac{3}{4}\mathbf{U}^n + \frac{1}{4}\mathbf{U}^{n,1} + \frac{1}{4}\Delta t M^{-1} L(\mathbf{U}^{n,1}),\\
\mathbf{U}^{n,3} &= \frac{1}{3}\mathbf{U}^n + \frac{2}{3}\mathbf{U}^{n,2} + \frac{2}{3}\Delta t M^{-1} L(\mathbf{U}^{n,2}),\\
\mathbf{U}^{n+1} &= \mathbf{U}^{n,3},
\end{aligned} \tag{2.12}$$

where $\mathbf{U}^{n,l}$, $l = 1, 2, 3$ are the solutions at the intermediate stages of the Runge–Kutta method.

### 2.4. Boundary treatment

Consider an interior element with an edge on the boundary of the computational domain, $\partial\Omega$. Denote this element by $E_b$ and the corresponding edge on the domain boundary as $e_b \in \partial E_b \bigcap \partial\Omega$. Consider the mirror element $E_m$ of $E_b$ as a reflection of $e_b$ outside of the computational domain, such that $\partial E_m \bigcap \partial E_b = e_b$ (see Fig. 1(a)).

On the boundary $\partial\Omega$ physical and artificial boundary conditions must be imposed. The boundary conditions determine the flux through the boundary edge $e_b$. This flux is computed through the numerical flux function

$$h(\mathbf{u}_h^{in}, \mathbf{u}_h^{out}, \mathbf{n}), \tag{2.13}$$

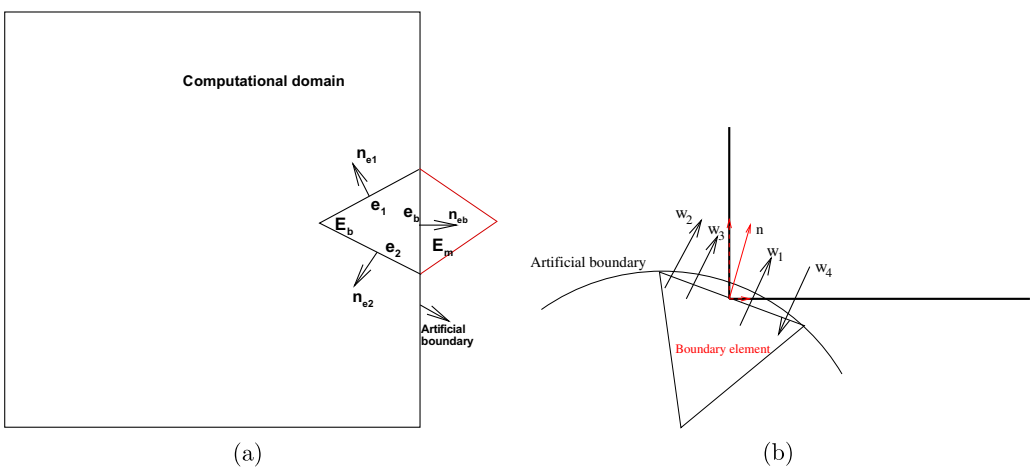


**Fig. 1.** (a) Boundary and mirror element. (b) The direction of the characteristic waves for a subsonic outflow boundary.

where $\mathbf{u}_h^{in} = \mathbf{u}_h|_{E_b}$ is the interior solution coming from the boundary element and $\mathbf{u}_h^{out} = \mathbf{u}_h|_{E_m}$ is the boundary data information that needs to be specified at the edge $e_b$ of the mirror element. For certain cases, physical boundary conditions may be used to determine the components of the flux through the boundary or the components of $\mathbf{u}_h|_{E_m}$. For example, for a solid wall the normal flux is zero. However, in general, analytic boundary conditions do not exist at the inflow and outflow boundaries, thus the values of $\mathbf{u}_h|_{E_m}$, are determined through specification of artificial boundary conditions.

## 3. Characteristic boundary conditions

The construction of ABCs for time depended problems is not an easy task, since ABCs must mimic the behavior of the *exact* data on the boundary. Furthermore, ABCs on the artificial boundaries (and their discretization) must prevent generation of numerical reflected waves, propagated back into the computational domain, in order to preserve stability and retain the overall accuracy of the numerical scheme.

An effective way to construct ABCs is by utilizing the characteristic theory. In the last few years, characteristic type ABCs, hereafter denoted as CHBC, have been proposed by many investigators [2,12,26]. In [11,17,18], CHBC were developed and applied for the numerical solution of the Euler and Navier–Stokes equations with finite difference methods for simple boundaries. In the following section, we generalize this technique for the DG framework and for boundaries of arbitrary shape. First, by applying characteristic analysis on $E_m$, an auxiliary hyperbolic type system is constructed for the incoming–outgoing waves. Next, by discretizing this system with the DG methodology an ODE system for the degrees of freedom of the waves is obtained. Finally, by expressing the degrees of freedom of the state variables (conservative variables) in relation the corresponding degrees of freedom of the waves the numerical scheme on the boundary is completed.

### 3.1. The characteristic system

The quasi-linear form of the system (2.1) for the element $E_m$ is,

$$\partial_t \mathbf{u} + A\partial_x \mathbf{u} + B\partial_y \mathbf{u} = 0, \tag{3.1}$$

where $A$, $B$ are the Jacobian matrices of the fluxes $\mathbf{f}$, $\mathbf{g}$ defined as

$$A = \frac{\partial \mathbf{f}}{\partial \mathbf{u}}, \quad B = \frac{\partial \mathbf{g}}{\partial \mathbf{u}}. \tag{3.2}$$

Let, $\mathbf{n} = (n_x, n_y)$, be the unit outward normal vector to the boundary edge $e_b$, see Fig. 1(b). We construct the matrix $R = R(\mathbf{n})$, [27], which diagonalizes the matrix $A\, n_x + Bn_y$. Hence,

$$\Lambda = R^{-1}(An_x + Bn_y)R \tag{3.3}$$

is the diagonal eigenvalue matrix whose diagonal entries are

$$\begin{aligned} \lambda_1 &= \mathbf{v}\cdot\mathbf{n}, \\ \lambda_2 &= \mathbf{v}\cdot\mathbf{n}, \\ \lambda_3 &= \mathbf{v}\cdot\mathbf{n} + c, \\ \lambda_4 &= \mathbf{v}\cdot\mathbf{n} - c \end{aligned} \tag{3.4}$$

where $c = \sqrt{\gamma p/\rho}$ is the local speed of sound. The right and left eigenvector matrices $R$, $R^{-1}$ relate variations of the conservative variables to variations of the characteristic variables $\mathbf{w}$ through the relations

$$\delta(\mathbf{w}) = R^{-1}\delta(\mathbf{u}), \quad \delta(\mathbf{u}) = R\delta(\mathbf{w}). \tag{3.5}$$

The characteristic waves, $w_i$, $i = 1,\ldots,4$ which cross the boundary edge $e_b$ (see Fig. 1(b) in case of a subsonic outflow boundary), have the form [27]:

$$\begin{aligned} \delta(w_1) &= \delta\rho - \tfrac{1}{c^2}\delta p, \\ \delta(w_2) &= n_y\delta u - n_x\delta v, \\ \delta(w_3) &= n_x\delta u + n_y\delta v + \tfrac{1}{\rho c}\delta p, \\ \delta(w_4) &= -n_x\delta u - n_y\delta v + \tfrac{1}{\rho c}\delta p \end{aligned} \tag{3.6}$$

with corresponding speeds $\lambda_i$ given by (3.4). The right and left eigenvector matrices $R$, $R^{-1}$ (see Eq. (3.3)) are associated with the normal to the boundary edge direction $\mathbf{n}$. As a result, the characteristic waves $w_i$, $i = 1, 2, 3, 4$ are functions of $\mathbf{n}$.

We multiply (3.1) by the left eigenvector matrix $R^{-1}$ and after some algebra, we obtain the following hyperbolic type system for the characteristic waves,

$$\begin{aligned}
&\left(\frac{\partial}{\partial t}+\mathbf{v}\cdot\nabla\right)w_1=0,\\
&\left(\frac{\partial}{\partial t}+\mathbf{v}\cdot\nabla\right)w_2=\frac{c}{2}(n_x\partial_y-n_y\partial_x)(w_3+w_4),\\
&\left(\frac{\partial}{\partial t}+(\mathbf{v}+c\mathbf{n})\cdot\nabla\right)w_3=c(n_x\partial_y-n_y\partial_x)w_2,\\
&\left(\frac{\partial}{\partial t}+(\mathbf{v}-c\mathbf{n})\cdot\nabla\right)w_4=c(n_x\partial_y-n_y\partial_x)w_2
\end{aligned}\tag{3.7}$$

Denoting as $\mathbf{F}_w$ and $\mathbf{G}_w$ the fluxes of the left and the right side of (3.7), respectively, the system (3.7) is written in compact form as

$$\frac{\partial}{\partial t}\mathbf{w}+\mathbf{F}_w=\mathbf{G}_w.\tag{3.8}$$

The right hand side of (3.8) expresses the variation of the waves along the tangential to the boundary direction $\mathbf{s}=(n_y,-n_x)$. Following the approach applied for the interior Riemann solver, where the normal to the interface flux is evaluated, the right-hand side tangential flux $\mathbf{G}_w$ of the system (3.8) is neglected and the following equation for the evaluation of the characteristic waves $w_i$ on $E_m$ is obtained:

$$\partial_t\mathbf{w}+\mathbf{F}_w=0.\tag{3.9}$$

The system (3.9) is referred to as the *characteristic system*, CHS.

By the last Eq. (3.9) and Eq. (3.5) we obtain

$$\partial_t\mathbf{u}+R\mathbf{F}_w=0,\tag{3.10}$$

$B(u(x,y,t))=0.$

which is the analytical evolutionary-type form of the boundary conditions (2.5) for the conservative state variables.

In the numerical implementation, however, we discretize system (3.9) to time advance the characteristic variables and use (3.5) to obtain the conservative variables. The (3.9) is solved numerically for all mirror elements of the artificial boundary, according to an upwind discretization in order to obtain a discrete approximation of the time variation of the waves $\partial_t\mathbf{w}|_{E_m}$, which cross the artificial boundary through the edges $e_b$. Our goal is to relate the discrete time variation of the waves (as we did in (3.10)) with the corresponding discrete time variation of the conservative variables.

In order to assess the importance of the right hand side term $\mathbf{G}_w$ of Eq. (3.8), numerical tests including that term were performed. These tests had shown negligible differences between the computed results. Therefore this term was neglected in the numerical examples which are presented in the next section. The development of characteristic based BC's for the linearized Euler equations is shown in Appendix A.

### 3.1.1. Discrete formulation of the CHS

For the discretezation of the CHS we can not apply the same procedure as in the original system (2.1). This is because for the mirror element, we wish to consider only one adjacent interior element, the boundary element. The flux $\mathbf{F}_w$ of the CHS in Eq. (3.9) has not the same form as the fluxes $\mathbf{f}$, $\mathbf{g}$ of the system of the Euler equations. Ignoring boundary terms and applying the finite element discretezation, the discrete analogue of (3.9) on $E_m$ is: find $\mathbf{w}_h\in V_h(E_m)$ such that,

$$\int_{E_m}\frac{\partial\mathbf{w}_h}{\partial t}\varphi\,dx\,dy=-\int_{E_m}\mathbf{F}_w(\mathbf{w}_h)\varphi\,dx\,dy,\quad\forall\varphi\in V_h(E_m).\tag{3.11}$$

For each of the equations of the CHS (see (3.7)), the *characteristic lines* are defined to be tangent to $\mathbf{l}_1=\mathbf{l}_2=\mathbf{v}$, $\mathbf{l}_3=\mathbf{v}+c\mathbf{n}$, $\mathbf{l}_4=\mathbf{v}-c\mathbf{n}$. The boundary edge $e_b$ is an *inflow boundary part* when $\lambda_i=\mathbf{l}_i\cdot\mathbf{n}>0$ for the $\partial E_m$, then waves $w_i$ propagate along the characteristic lines form $E_b$ towards $E_m$. We apply an upwind discretization for (3.9) and ensure communication between $\mathbf{u}_h|_{E_b}$ and $\mathbf{u}_h|_{E_m}$ by introducing the following jumps on $e_b$

$$\mathbf{l}_i\cdot\mathbf{n}R^{-1}(\mathbf{u}_h|_{E_b}-\mathbf{u}_h|_{E_m})=\lambda_iR^{-1}(\mathbf{u}_h|_{E_b}-\mathbf{u}_h|_{E_m})\tag{3.12}$$

to the discrete formulation (3.11). (However, when $\lambda_i=\mathbf{l}_i\cdot\mathbf{n}<0$ the edge $e_b$ is inflow part for $\partial E_b$ and we set the jump terms to have the form $\mathbf{l}_i\cdot(-\mathbf{n})R^{-1}(\mathbf{u}_h|_{E_m}-\mathbf{u}_h|_{E_b})$, coinciding with (3.12)). The solution $\mathbf{w}$ of (3.9) is obtained, with the discontinuous Galerkin method by $\mathbf{w}_h\in V_h(E_m)$ such that,

$$\int_{E_m}\frac{\partial\mathbf{w}_h}{\partial t}\varphi\,dx\,dy=-\int_{E_m}\mathbf{F}_w(\mathbf{w}_h)\varphi\,dx\,dy+\int_{e_b}\Lambda(\mathbf{u}_h|_{E_b},\mathbf{u}_h|_{E_m})R^{-1}(\mathbf{u}_h|_{E_b},\mathbf{u}_h|_{E_m})(\mathbf{u}_h|_{E_b}-\mathbf{u}_h|_{E_m})\varphi\,ds,\quad\forall\varphi\in V_h(E_m),\tag{3.13}$$

where $\Lambda$, $R^{-1}$ are evaluated at the Roe's average state on the midpoint of $e_b$. Note that (3.13) is a straightforward extension of the Lesaint and Raviart upwind scheme [28] in our case (see also [29]), however, the linear case method proposed in [30, chapter 9, pp. 168,169, 189–195], is applied. The discretization method can be considered as a high order upwind method and the proposed boundary treatment becomes analogous to the high order extrapolation approach used by Nordström in the finite difference context [31,32].

Replacing $\varphi$ in (3.13) by the polynomials of the base of $V_h(E_m)$, we obtain a system of ODE's for the degrees of freedom $\mathbf{W}$ of the numerical solution $\mathbf{w}_h$ of the characteristic waves,

$$\frac{d\mathbf{W}}{dt} = \mathcal{L}_{E_m}(\mathbf{w}_h), \tag{3.14}$$

where the right hand side $\mathcal{L}_{E_m}$ is the right hand side of (3.13) multiplied by the inverse mass matrix $M^{-1}$.

The variation of the degrees of freedom of the conservative variables is related to the variation of the degrees of freedom of the characteristic waves through relations (3.5). After substitution of (3.5) in (3.14) obtain the following system of ODE's,

$$\frac{d\mathbf{U}}{dt} = R\frac{d\mathbf{W}}{dt} = R\mathcal{L}_{E_m}(\mathbf{w}_h) = \mathcal{L}_{bc}(\mathbf{w}_h)|_{E_m}, \tag{3.15}$$

where $R$ is computed at the Roe' average state on the midpoint of $e_b$ and $\mathbf{U}$ is the vector of the degrees of freedom of $\mathbf{u}_h|_{E_m}$, to be advanced in time.

The system (3.15) defines the semi-discrete analogue of the CHBC (3.10) (referred to as the CHBC–ODE system) and is advanced in time using the same Runge–Kutta method (2.12), with time step $\Delta\bar{t} = \min_{i=1,\dots,4}|\lambda_i|\Delta t$. We note that for the numerical solution of CHBC–ODE by the Runge–Kutta method, the characteristic waves (the right hand side) at the intermediate stages $l$, $l = 1, 2, 3$, are computed using the solution data from the previous stage $\mathbf{U}^{n,l-1}|_{E_m}$, see (2.12). The numerical solution obtained from (3.15) yields values of the conservative state variable vector $\mathbf{u}_h$ on the edge $e_b$ of the mirror element $E_m$. Using these values the numerical flux $h(\mathbf{u}_h|_{E_b}, \mathbf{u}_h|_{E_m}, \mathbf{n})$ (see (2.13)), on $e_b$ can be computed.

**Remark 3.1.** Characteristic waves leave and enter the computational domain through $e_b$ of the artificial boundary (see Fig. 1(b) for the subsonic flow case). For the construction of acceptable characteristic type boundary conditions, the waves must be computed in a consistent way. In Ref. [18], the outgoing waves were computed using upwind differencing, while the incoming waves were specified using information (or prescribing the behavior) of the solution outside the computational domain. In general, it is not possible to fix the labeling of the waves as incoming or outgoing in advance, since the sign of $\lambda_i$ may change in time, especially for time dependent flow problems.

As we mentioned previously, the present method evaluates all the waves from the solution $\mathbf{u}_h|_{E_m}$ of (3.15) obtained at the previous time step. As a result, the flux $\mathbf{F}_w(\mathbf{w}_h)$ of (3.13) is computed in the same way for both unsteady flow problems (where no information is available for the exterior problem outside of the domain) and for steady-state flow problems (where we can specify a primitive variable in $E_m$, for example $p = p_\infty$.) In both cases, control of strong reflected waves is achieved but generation of spurious numerical waves on the computational boundaries is not entirely eliminated.

## 4. Numerical examples

It is well known that the numerically generated reflected waves, caused by inexact inflow-outflow boundary conditions, could deteriorate the overall accuracy of the method. In order to evaluate the effect of the proposed artificial boundary conditions on the overall accuracy of the method, appropriate numerical examples for both steady and time dependent problems are performed.

First a time dependent problem the propagation of an isentropic vortex in a uniform stream is considered. Convection of a vortex through an artificial outflow computational boundary is a difficult time-depended test problem [16,32]. For this problem, boundary treatment procedures based on one-dimensional Riemann invariant extrapolation, usually fail. For this case, the flow near the boundary cannot be represented as a small amplitude disturbance to a uniform state and any artificial boundary treatment is not fully nonreflective. The convection of the isentropic vortex is governed by the Euler equations. For this problem, it is found that the incoming numerical waves generated by the application of CHBC's approach, slightly affect the overall accuracy of the numerical solution. Furthermore, the numerical perturbations generated by the incoming waves do not deteriorate the stability of the method.

The second problem is steady subsonic invicid flow over a cylinder at $u_\infty = 0.3$. It is well known that the approximation of the exact inviscid solution requires large number of elements and/or curved elements on the surface [33]. In order to demonstrate the effectiveness of the proposed BC we solve the problem using simple extrapolation BC's and 1D Riemann invariant BC's. Two computational domains are used, one extending 10 diameters away from the cylinder and a larger one extending 20 diameters away from the cylinder. In all cases, it was found that the characteristic BC ensure better stability than the other two extrapolation-type BC's.

We used the same boundary conditions for the numerical solution of aeroacoustic problems that are governed by the linearized Euler equations and involve only small variations of the state variables, even though the boundary conditions were developed for the nonlinear Euler equations. The first problem is the propagation of an aeroacoustic pulse ($p' = 0.01p_\infty$) that crosses the artificial boundary. This test problem has an analytical solution presented in [13]. The second problem is scattering of an acoustic pulse by a circular cylinder [23,34]. The last problem of this category has a time periodic solution and is the propagation of acoustic pulses generated by a time harmonic source [34]. These problems were solved using the full Euler equations. Although the method of artificial boundary conditions was not developed for the Navier–Stokes equations we ap-

ply the same technique for a viscous flow test case. This test problem is the subsonic flow ($u_\infty = 0.3$) past a circular cylinder at $Re = 200$.

In the numerical examples we denote the numerical solutions computed by the application of the proposed boundary treatment as *CHBC*. For certain problems where the exact solution is known, we also obtained numerical solutions using boundary values specified by the exact solution. The idea of using existing exact or semi-analytic BC at the computational boundaries has been exploited in the past [35,36]. It was demonstrated that the use of exact relations for the specification of the data at the computational boundaries yields accurate numerical solutions for computational domains of reduced size. Here analytical specification of boundary data is used for comparison. We denote the corresponding numerical solutions as *ExBc*. All the numerical examples have been performed using $V_h(E) = \mathbb{P}^3(E),\ \forall E \in T_h$ local polynomial space, for comparison reasons some test cases have been also solved using $V_h(E) = \mathbb{P}^k(E), k = 1, 2$ local space.

### 4.1. Isentropic vortex convection

The DG finite element method, with the proposed characteristic boundary conditions, is used for the convection of a vortex through the computational boundary. The domain is $\Omega = [0{:}10] \times [-10{:}10]$ and the outflow boundary $\Gamma_{outflow\ \mathrm{bd}} = \{(x,y)$: $x = 10,\ -10 \leqslant y \leqslant 10\}$. The free stream flow velocity, pressure, and density are prescribed as:

$$[\rho_\infty, u_\infty, v_\infty, p_\infty] = [1, 1, 0, 1].$$

The initial condition for the isentropic vortex is the addition of perturbations in the velocity components $(u, v)$ and temperature $T$ (no perturbation in entropy) to the free stream. These perturbations are given by:

$$(\delta u, \delta v) = \left(\frac{\beta}{2\pi} e^{\frac{1-r^2}{2}}(-y', x')\right), \tag{4.1}$$
$$\delta T = -\frac{(\gamma-1)\beta^2}{8\gamma\pi^2} e^{1-r^2},$$

where $\beta$ is the vortex strength, $\gamma = 1.4$, and $(x_{vo}, y_{vo})$ are the initial coordinates of the vortex center, $(x', y') = (x - x_v, y - y_v)$, and $r^2 = x'^2 + y'^2$. In the absence of viscous terms, the entire flow field is required to be isentropic, $\delta S = 0$, and the initial condition for the conservative state variables vector $\mathbf{u}(x,y,0) = \mathbf{u}_0$ is

$$\mathbf{u}_0 = \begin{bmatrix} \rho \\ \rho u \\ \rho v \\ \rho e \end{bmatrix} = \begin{bmatrix} (1+\delta T)^{\frac{1}{\gamma-1}} \\ \rho(u_\infty + \delta u) \\ \rho(v_\infty + \delta v) \\ \frac{p}{\gamma-1} + \frac{\rho(u^2+v^2)}{2} \end{bmatrix}. \tag{4.2}$$

The exact solution remains self similar for all times and represents a passive convection of the vortex with the freestream velocity $(u_\infty, v_\infty)$. In the numerical examples, the value $\beta = 2$ was used and vortex center was placed at $(x_{vo}, y_{vo}) = (8., 0)$. The numerical solution is computed on regular triangular meshes using grid spacing $\Delta h = 0.5$, 0.25, 0.125, 0.04 and $\mathbb{P}^k(E), k = 1, 2, 3$ local space. Fig. 2(a) shows the initial density field for discretization of the domain with $\Delta h = 0.5$. Fig. 2(b) shows that the entire flow-field is mixed-type subsonic/supersonic

$$\begin{cases} \frac{u}{c} < 1, & \text{for } y > 0 \\ \frac{u}{c} > 1, & \text{for } y < 0. \end{cases}$$

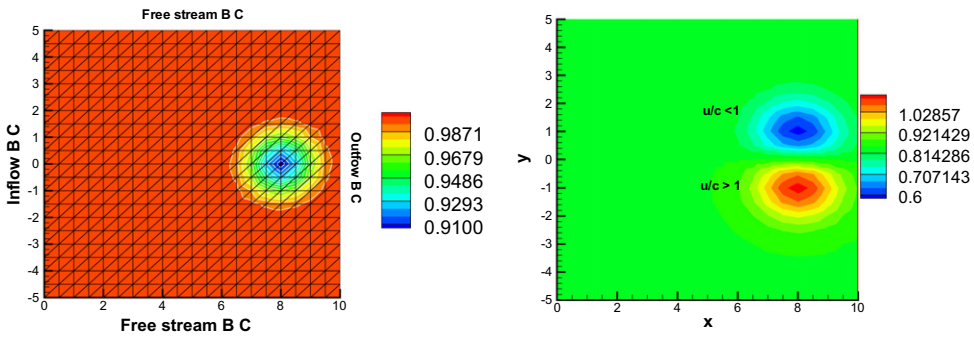


(a) Initial position of the vortex, density contours

(b) Contours of $u \lhd c$

**Fig. 2.** Vortex propagation through a subsonic outflow boundary, $\Delta h = 0.5$, $t = 0$.

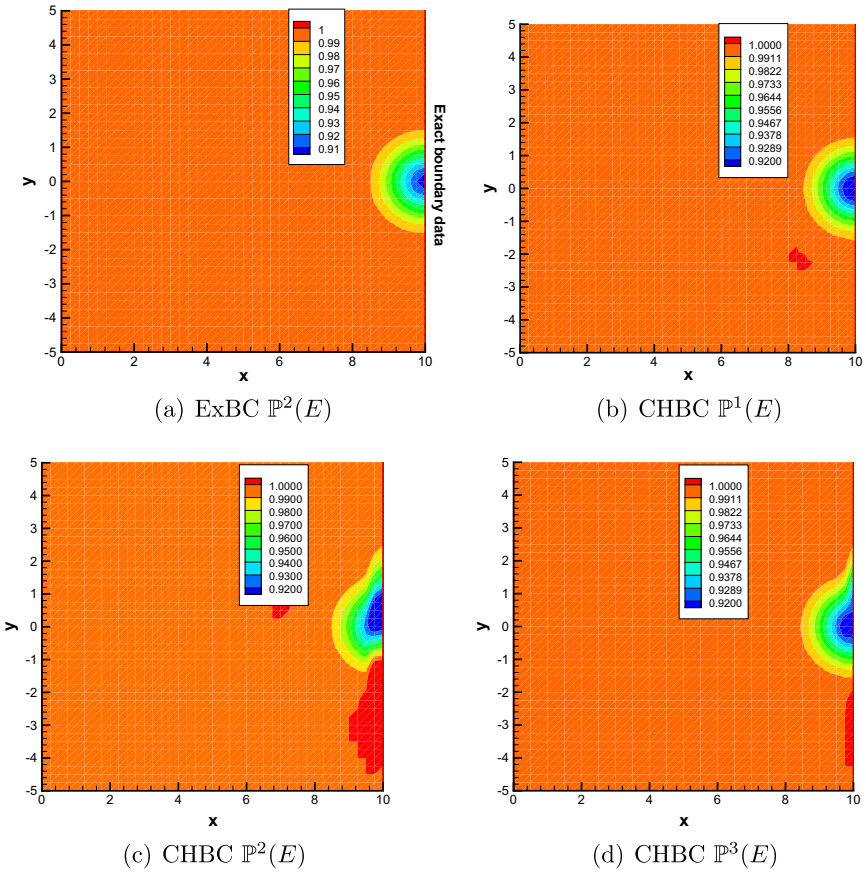


**Fig. 3.** Vortex problem. Half vortex has crossed the subsonic outflow boundary boundary. Density contours at $t = 2$ omputed on mesh $\Delta h = 0.25$ with $\mathbb{P}^k(E),\ k = 1, 2, 3$ local space, (a) ExBC, (b)–(d) CHBC.

Time iterations start and the vortex is convected downstream. At time $t = 2$ vortex center is located at (10,0) on the outflow boundary and half vortex has passed through the artificial boundary out of the computational domain. Fig. 3 shows, the crossing of the vortex to the outflow boundary, at $t = 2$, for grid size $\Delta h = 0.25$ using local space $\mathbb{P}^k(E), k = 1, 2, 3$. In Figs. 3(b)–(d) CHBC have been used and in Fig. 3(a) the boundary values have been specified from the analytic solution (ExBC). It is seen, Figs. 3(c) and (d), that the shape of the vortex for $\mathbb{P}^k, k = 2, 3$ polynomial space has been deformed, while the deformation of the vortex corresponding to the more diffusive $\mathbb{P}^1$ local space is less pronounced.

The vortex continues to escape through the outflow boundary and for a later time, $t = 4$, the vortex has moved out of the computational domain. However, Fig. 4 shows that perturbations (reflected waves) generated during the passage of the vortex through the outflow boundary remain in the computational domain. As mentioned earlier, we are interested in preserving high order accuracy for long time integration. A criterion for assessing the quality of the proposed ABC is considered and is established. This criterion is related to the magnitude of the numerical reflected waves. The behavior of the reflected waves depends on the discrete spatial operator, and as shown in Fig. 4, the amplitude of these waves increases with the order of the scheme. In the case of linear advection and linearized Euler equations, an analysis of the reflected waves form for high-order finite difference schemes is given in [18] (and the references therein, see also [37]). Based on appropriate numerical experiments, we show that the reduction of the perturbations for certain degree of the local polynomial space is achieved by decreasing the mesh size. Thus, first we explore the effect of the reflected waves on the accuracy of the method by performing the following comparison. At time $t = 4$ the $L_2$ error of the density variable

$$\|\rho_h - \rho_{exact}\|_2 = \sqrt{\sum_{E \in T_h} \int_E (\rho_h - \rho_{exact})^2 dx\, dy},$$

is computed for the different size meshes. The grid convergence rate of the $L_2$ error for $\mathbb{P}^k, k = 1, 2, 3$ is shown in Fig. 5. In Fig. 5(a), the convergence rate of the $L_2$ error using characteristic BC versus grid size, $\Delta h$, is presented. The convergence rate using exact boundary data specified by the analytical solution (ExBC) is shown in Fig. 5(b). Note that the error level for lower order approximations is smaller due to the more diffusive nature of the low order schemes. However, the rate of reduction of the error is consistent with the order of the scheme for both CHBC and ExBC. It is observed that the reduction rate of the error

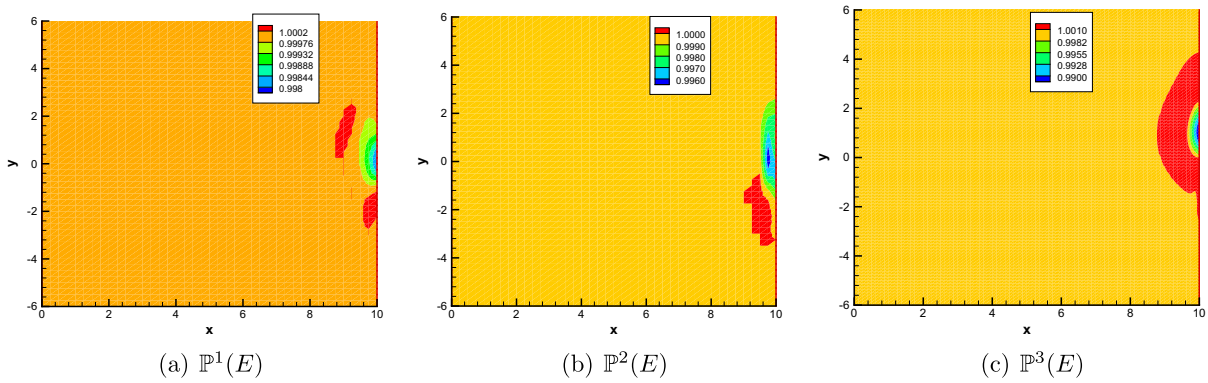


(a) $\mathbb{P}^1(E)$ (b) $\mathbb{P}^2(E)$ (c) $\mathbb{P}^3(E)$

**Fig. 4.** Vortex problem. Remaining perturbations of density field on mesh $\Delta h = 0.25$ at $t = 4$. The vortex has left the computational domain and spurious numerical waves generated by the crossing on the vertical boundary.

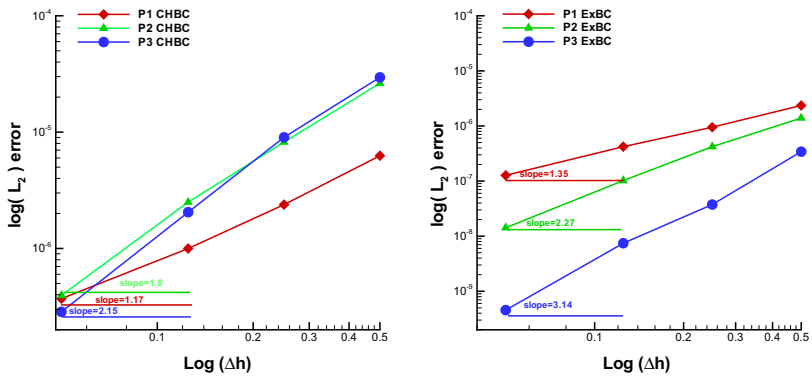


(a) CHBC (b) ExBc

**Fig. 5.** Vortex problem. The convergence rate of the $L_2$ error of the density, in case of (a) CHBC and (b) ExBc.

of the characteristic BC is 1.3% (for $\mathbb{P}^3$ 1.4%) less than the corresponding reduction rate of the ExBC. The comparison of Figs. 5 leads to the conclusion that, the proposed BC are able to retain the high order accuracy of the scheme, and the numerical reflected waves do not dramatically affect the accuracy of the method to the degree that the boundary condition treatment is unacceptable, even for an extreme case such as the outgoing vortex.

Next, we demonstrate the reduction rate of the magnitude of the reflected waves, $\sigma$, with the grid spacing for $\mathbb{P}^k, k = 1, 2, 3$. The reflected waves magnitude is estimated by the relation

$$\sigma = |L_2(CHBC) - L_2(ExBC)|.$$

Both $L_2$ errors include space and time discretizations errors and $\sigma$ can be considered as a *measure* of the magnitude of the reflected waves. Fig. 6 displays the reduction rate of the $\sigma$ with the grid size for $\mathbb{P}^k, k = 1, 2, 3$ at $t = 4$. We observe that the reduction rate of the magnitudes is very close to the rate of the $L^2$ error (see Fig. 5(a)). Since the CHBC retain high order accuracy, we can conclude that: despite the fact that for coarse meshes the magnitude of the reflected waves generated for $\mathbb{P}^3(E)$ local space is greater than the corresponding reflected waves magnitude of $\mathbb{P}^1(E)$, by refining successively the mesh, finally the reflected waves generated in case of $\mathbb{P}^3(E)$ space become weak.

For small disturbance numerical solutions of the Euler equations (see aeroacoustic problems in the next section) it will be shown that the reflected waves are very weak, since the computational results show that point values of the CHBC solutions are very close to the point values of the ExBC solutions, as well the convergence rate of the $L_2$ error is close to the expected theoretical rate. This numerical test case is *more stringent* than the aeroacoustic problems, however, Figs. 5 and 6, indicate that use of the proposed CHBC yields high resolution results even for *complex flow* problems.

### *4.2. Steady state numerical test*

The proposed characteristic BC's have been applied for the computation of inviscid subsonic flow over a cylinder for a free stream speed $u_0 = 0.3$. The cylinder has unit diameter. The circumference of the cylinder is discretezed with 40 elements. The artificial boundary is placed 10 diameters (10D) away from the cylinder surface and is also discrtitized using 40 elements. A

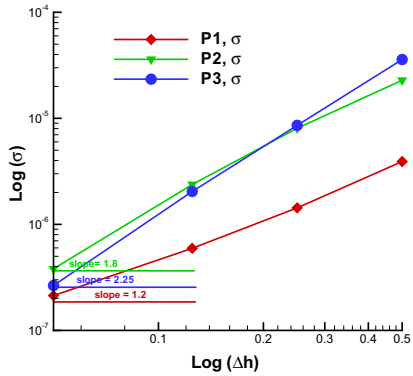


**Fig. 6.** Vortex problem. Reduction rate of the perturbation magnitudes $\sigma$ with the grid refinement in relation to the local space at $t = 4$.

regular triangular mesh is used and the local polynomial space is $V_h(E) = \mathbb{P}^3(E),\ \forall E \in T_h$. For comparison, computations where BC's were prescribed by applying simple one-dimensional extrapolation BC and use of Riemann invariants in a direction normal to the boundary were carried out. In the first case, the variables $\rho$, $u$, $v$ were extrapolated by setting to the outflow mirror element $E_m, \rho_h|_{E_m} = \rho_h|_{E_b},\ u_h|_{E_m} = u_h|_{E_b},\ v_h|_{E_m} = v_h|_{E_b}$ and the pressure was held constant $p_h|_{E_m} = p_\infty$. In the second case, the primitive variables are obtained by Riemann invariants. The problem was solved at final time $t = 20$. Comparisons between numerical solutions obtained with CHBC, extrapolated BC (Extr BC) and by Riemann invariants (RI BC) shows the effectiveness of the CHBC against the other two. Fig. 7(a)–(c) show the Mach isolines computed using CHBC, Extr BC, and Rieman invariant, RI BC, respectively. The spurious waves that appear when extrapolation BC are used (see Fig. 7(b)) are eliminated when CHBC (see Fig. 7(a)) are used.

Next the computational domain is expanded and the outflow boundary is placed 20 diameters (20D) away from the cylinder. The numerical solution is obtained using extrapolated BC. The Mach isolines are shown in Fig. 7(d). For all numerical solutions shown in Fig. 7(a)–(d) the $L_2$ norm of the density residual

$$L_2(\rho_h, residual) = \sum_{E \in T_h} \sqrt{\int_E (\rho_h^{n+1} - \rho_h^n)^2 dx\, dy}$$

was recorded. For the computation with the expanded (20D domain), the norm has been recorded only on the elements which are included in the 10 diameters circle away from the cylinder. The variation of the $L_2(\rho_h, residual)$ versus time, presented in Fig. 7(e), clearly demonstrates that the application of the characteristic BC enables the convergence to a steady-state solution for the 10D domain. On the contrary, the other two methods do not. Therefore, for this steady-state problem, application of the characteristic BC provides a more appropriate numerical boundary treatment compared to the extrapolated and Riemann invariant BC.

### 4.3. Performance of CHBC for aeroacoustic problems

#### 4.3.1. Propagation of Gaussian pulse

Next, the proposed boundary conditions are tested for aeroacoustic-type problems. These problems have been solved numerically in [13] using a high order finite difference methods. Here, we solve these problems using $V_h(E) = \mathbb{P}^3(E),\ \forall E \in T_h$ local space. In order to test the stability of the CHBC for aeroacoustic problems, we perform comparisons between point values of the CHBC numerical solutions and the corresponding point values of the numerical solutions produced with the exact boundary values specified by the analytical solution (ExBC). For both numerical solutions the $L_2$ error is computed.

We solve the nonlinear Euler equations for small amplitude disturbances using the same code used for the inviscid simulations of the previous problems. For disturbances with sufficiently small magnitude the numerical solutions of the full Euler equations may be compared with the analytic solutions for the linear problem [13].

The propagation of a Gaussian pulse in the presence of a uniform mean flow is the first test problem. The computational domain is $\Omega = [-5{:}5] \times [-8{:}8]$ with $\Gamma_{outflow\ \mathrm{bd}} = \{(x,y)\colon x = 5, -8 \leqslant y \leqslant 8\}$. We perform four triangulations of $\Omega$ into equally spaced triangular elements with grid size $\Delta h_i = 0.1, 0.2, 0.4, 0.8$, $i = 1, 2, 3, 4$. At time $t = 0$ an acoustic pulse is generated on the center of the computational domain. The initial field and the acoustic disturbances are,

$$\begin{bmatrix} \rho_0 \\ u_0 \\ v_0 \\ p_0 \end{bmatrix} = \begin{bmatrix} 1. \\ M_x \\ M_y \\ \frac{1}{\gamma} \end{bmatrix},$$

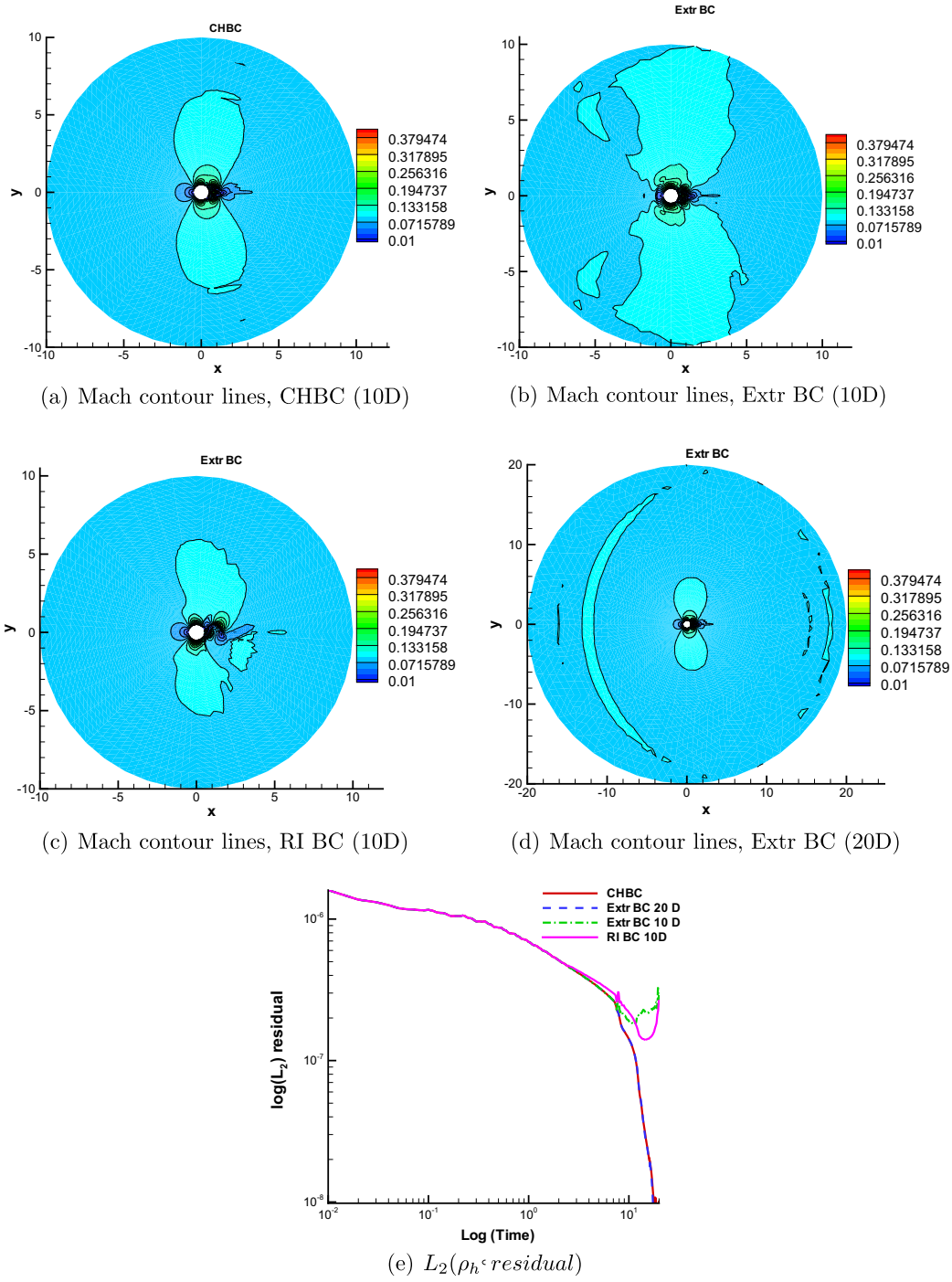


(a) Mach contour lines, CHBC (10D)

(b) Mach contour lines, Extr BC (10D)

(c) Mach contour lines, RI BC (10D)

(d) Mach contour lines, Extr BC (20D)

(e) $L_2(\rho_h$‘$residual)$

**Fig. 7.** Mach isolines computed using $V_h(E) = \mathbb{P}^3(E)$. (a) CHBC on the artificial boundary located 10 diameters away from the cylinder, (b) Extrapolated BC on the artificial boundary located 10 diameters away from the cylinder, (c) Riemann invariants BC on the artificial boundary located 10 diameters away from the cylinder, (d) Extrapolated BC on the artificial boundary located 20 diameters away from the cylinder, (e) the variation of the $L_2(\rho_h, residual)$ for the (a)–(d) numerical computations.

$$\rho' = \varepsilon \exp(-ln(2)(x^2 + y^2))$$
$$u' = 0.$$
$$v' = 0.$$
$$p' = \varepsilon \exp(-ln(2)(x^2 + y^2))$$

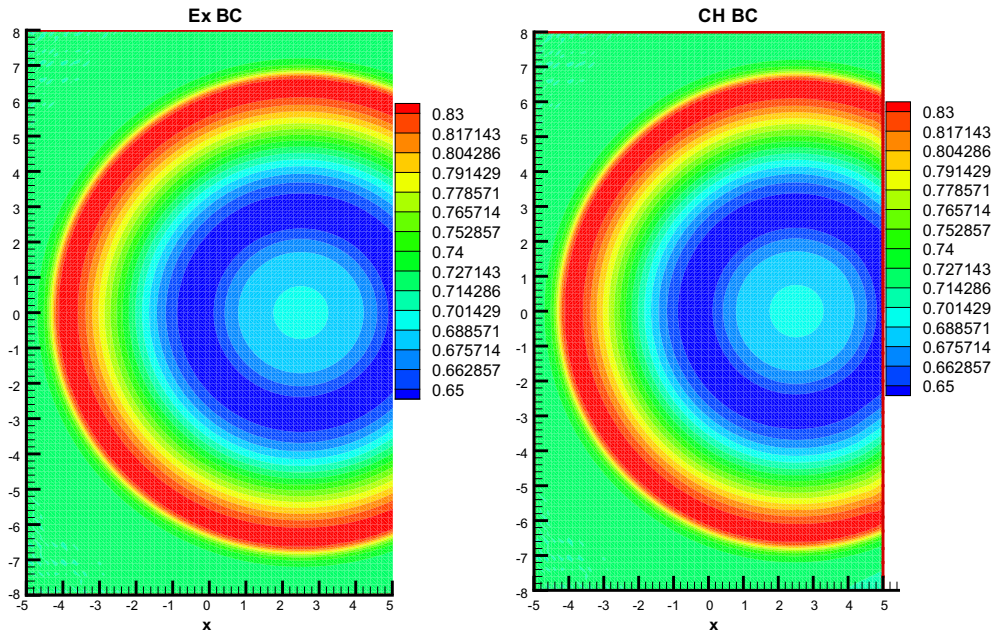


**Fig. 8.** Pulse propagation problem, $V_h(E) = \mathbb{P}^3(E)$. Pressure contours at $t = 5$, right: CHBC are imposed on the outflow boundaries, left: ExBC are imposed on the outflow boundaries.

where in the numerical experiments we set $M_x = 0.5$, $M_y = 0$, $\varepsilon = 0.01$. As time elapses the pulse spreads. Simultaneously due to the mean flow the whole pattern convects downstream. The pulse crosses the $\Gamma_{outflow\ \mathrm{bd}}$ and escapes from the computational domain. At time $t = 5$, for the triangulation $\Delta h_1$ the pressure contours are shown in Fig. 8 using characteristic BC and BC specified by the exact solution (ExBC). The grid convergence rate of the $L_2$ error using CHBC and ExBC is shown in Fig. 9. The comparison of the two convergence rates in Fig. 9 shows that the application of the CHBC does not deteriorate the accuracy of the numerical method. In Fig. 10(a) and (b), comparisons of the pressure distributions obtained for $\Delta h_1$ along the X-axis and Y-axis is presented. Good agreement between the CHBC and ExBC solutions is observed. It is therefore concluded that the reflected waves are weak and do not affect the quality of the numerical solution.

The next numerical example is the propagation of the acoustic pulse simultaneously with a vortex convection [13]. The computational domain is $\Omega = [-100{:}100] \times [-100{:}100]$ and is subdivided in triangular elements with size $\Delta h = \Delta x = \Delta y = 1$. An acoustic pulse is generated by an initial Gaussian pressure distribution at the center of the $\Omega$. In addition, a vortex is generated by a Gaussian distribution with center at the point (67,0). The initial disturbances are given by the following relations:

$$\rho' = \varepsilon_1 \exp\left(-\frac{ln(2)}{9}(x^2+y^2)\right) + \varepsilon_2 \exp\left(-\frac{ln(2)}{25}((x-67)^2+y^2)\right),$$

$$u' = \varepsilon_3 y \exp\left(-\frac{ln(2)}{25}((x-67)^2+y^2)\right),$$

$$v' = -\varepsilon_3 (x-67) \exp\left(-\frac{ln(2)}{25}((x-67)^2+y^2)\right),$$

$$p' = \varepsilon_1 \exp\left(-\frac{ln(2)}{9}(x^2+y^2)\right)$$

where the following constant values $\varepsilon_1 = 0.01$, $\varepsilon_2 = 0.001$, $\varepsilon_3 = 0.0004$ were used. The mean flow Mach number is taken equal to 1. Time iterations start and the center of the pulses are moving downstream. At a letter time the pulses cross the outflow boundary $\Gamma_{outflow\ \mathrm{bd}} = \{x = 100, -100 \leqslant y \leqslant 100\}$. Fig. 11 shows the pressure distributions at time $t = 60$ using CHBC and exact boundary data, ExBC. Clearly, only reflections of negligible size appeared due the application of the characteristic boundary conditions.

The computed pressures at $t = 60$ for the points $X_i = -100 + (i-1)\Delta x$, $i = 1,\ldots,201$ along $X$-axis and for the points $Y_i = -100 + (i-1)\Delta y$, $i = 1,\ldots,201$ along the outflow boundary $\{x = 100, -100 < y < 100\}$ are compared in Fig. 12. In order

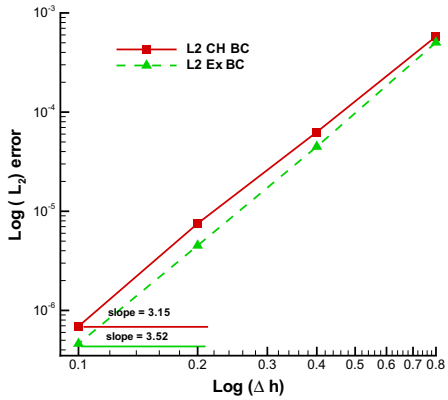


**Fig. 9.** Pulse propagation problem, $V_h(E) = \mathbb{P}^3(E)$. The $L_2$ convergence rates using CHBC and ExBC.

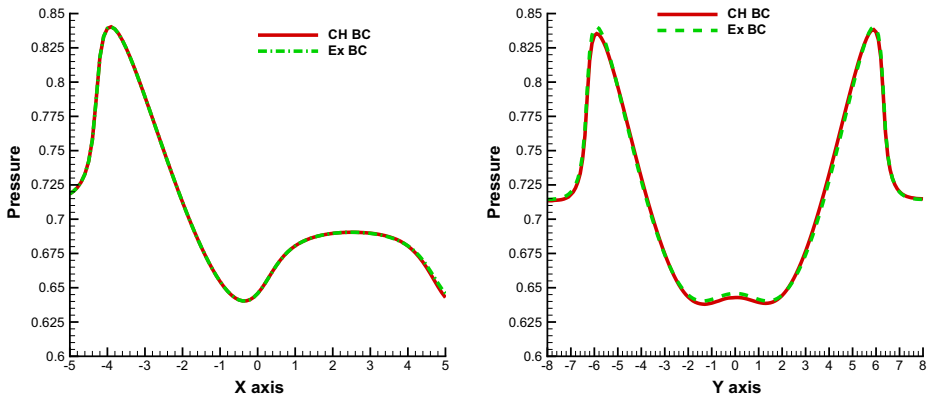


(a) X-axis (b) Outflow boundary

**Fig. 10.** Pulse propagation problem, $V_h(E) = \mathbb{P}^3(E)$. Pressure profiles on $X$-axis and on the outflow boundary $\{x = 5, -8, y < 8\}$ using CHBC and ExBC.

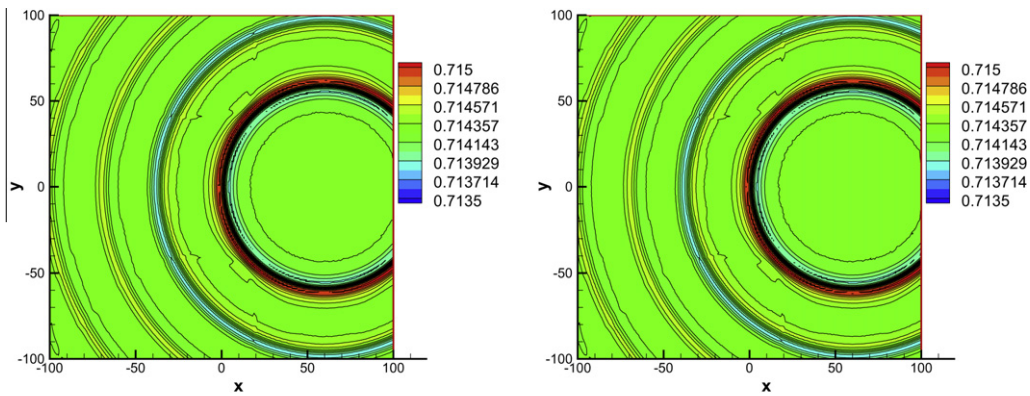


(a) CHBC (b) ExBC

**Fig. 11.** Pulse-vortex problem, $V_h(E) = \mathbb{P}^3(E)$. Pressure contours using CHBC and ExBC at $t = 60$.

to estimate the magnitude of the reflected waves generated due to the application of the proposed CHBC, we compute the difference between the exact pressure values and (i) the pressure values computed using CHBC (*Exact* − *CHBC*), (ii) using ExBC (*Exact* − *ExBc*) for the points along the $X$-axis. The results are displayed in Fig. 13. The magnitude of the difference *Ex-*

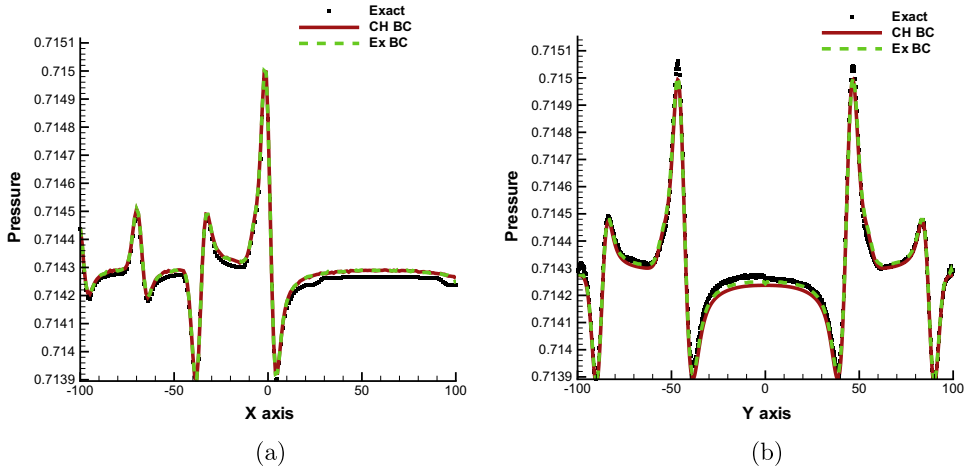


**Fig. 12.** Pulse-vortex problem, $V_h(E) = \mathbb{P}^3(E),\ t = 60$. (a) Comparison of the pressure values on the points of the $X$-axis (b) Comparison of the pressure values on the points of the outflow boundary ($x = 100, -100 < y < 100$).

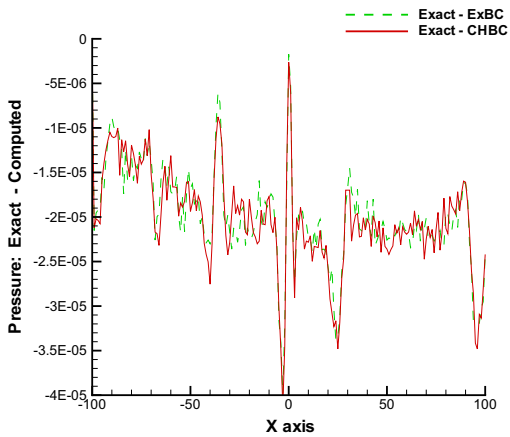


**Fig. 13.** Pulse-vortex problem, $V_h(E) = \mathbb{P}^3(E),\ t = 60$. The deference of the pressure values Exact – CHBC and Exact – ExBC for the points of the $X$-axis.

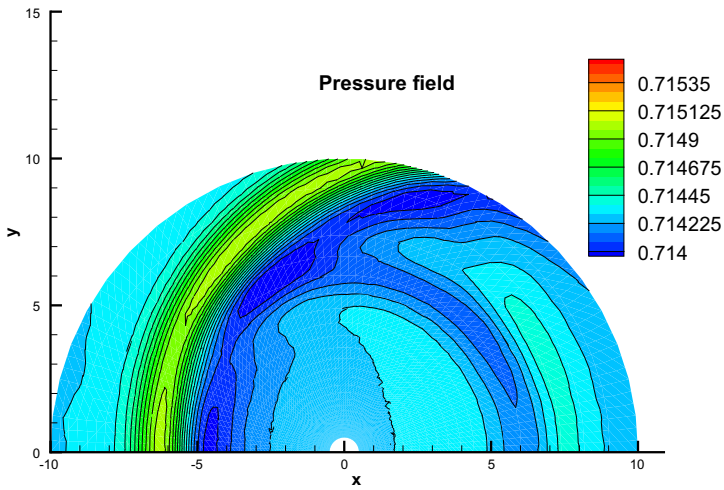


**Fig. 14.** Acoustic pulse scattering problem, $V_h(E) = \mathbb{P}^3(E)$. The final pressure field at $T = 8$ computed on the fine mesh using the characteristic boundary conditions on the outflow boundary.

*act* − *CHBC* remains very close to the difference *Exact* − *ExBc* for all the points of the *X*-axis. Therefore it appears that for acoustic wave propagation the numerically generated waves do not damage the quality of the numerical solution. For the numerical solution of the aeroacoustic problems, we tried to implement the radiation boundary conditions proposed in [13] following the same procedure as in Section (3.1.1). Their performance was worse than the results obtained for CHBC's.

*4.3.2. Scattering of an acoustic pulse by a cylinder surface*

Scattering of an aeroacoustic pulse by the surface of a circular cylinder is considered next. The center of the cylinder is $(x,y) = 0.0$ and its radius $r = 0.5$. The outflow boundary part of $\Omega$ is the hemicycle $\Gamma_{outflow\ bd} = \{(x,y) : \sqrt{x^2+y^2} = 10, y \geqslant 0\}$. The rigid boundary is the upper half of the surface of the cylinder $\Gamma_{cyl} = \{(x,y) : \sqrt{x^2+y^2} = 0.5, y \geqslant 0\}$ and the points $\{(x,y), -10 \leqslant x \leqslant 0.5, y = 0\} \bigcup \{(x,y), 0.5 \leqslant x \leqslant 10, y = 0\}$. The pulse is introduced by the initial pressure disturbance centered at $(x,y) = (4,0)$. The initial conditions are

$$\mathbf{u}_0 = \begin{pmatrix} \rho_0 = 1 \\ u_0 = 0 \\ v_0 = 0 \\ p_0 = \varepsilon \exp\left(-\frac{ln(2)}{w}((x-4)^2 + y^2)\right) \end{pmatrix},$$

in the numerical experiments we set the Gaussian half-width $w = 1$ and $\varepsilon = 0.01$. Further details on the set up of this problem can be found in [23]. For all the computations the local space is $V_h(E) = \mathbb{P}^3(E)$. Three triangular meshes with finer discretization of both the $\Gamma_{outflow\ \mathrm{bd}}$ and of the $\Gamma_{cyl}$ are used. For the coarse mesh the $\Gamma_{outflow\ \mathrm{bd}}$, $\Gamma_{cyl}$ are discretized by $N_{outflow\ \mathrm{bd}} = 6$ elements. For the medium mesh the surfaces are discretized using $N_{outflow\ \mathrm{bd}} = 12$ and for the fine mesh using $N_{outflow\ \mathrm{bd}} = 24$ elements. We can approximately consider that the size of the $\Gamma_{outflow\ \mathrm{bd}}$ discretization is $\Delta\Gamma_{outflowbd} = \frac{\Gamma_{outflowbd}}{N_{outflow\ bd}}$.

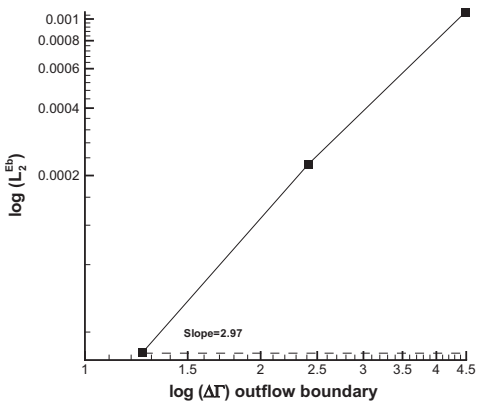


**Fig. 15.** Acoustic pulse scattering problem, $V_h(E) = \mathbb{P}^3(E)$. The converge rate of the $L_2^{E_b}$ error at $t = 8$.

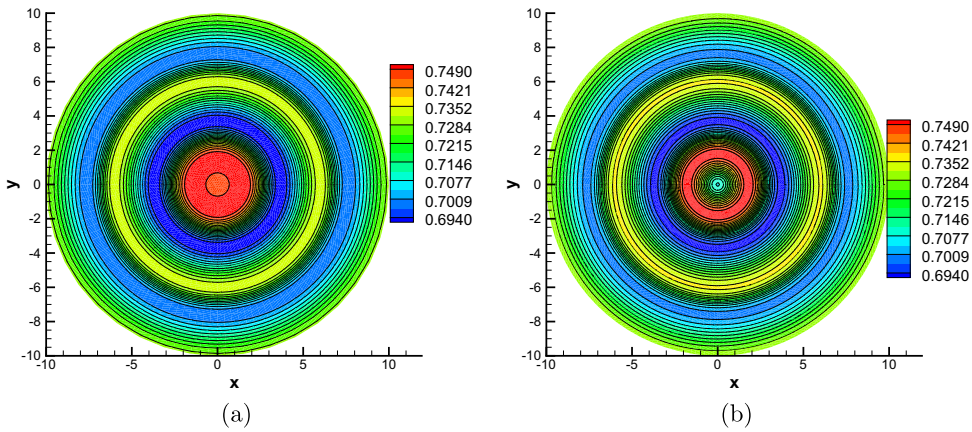


**Fig. 16.** Acoustic time harmonic source problem, $V_h(E) = \mathbb{P}^3(E)$. Comparison of computed pressure field at $t = 350$: (a) CHBC coarse mesh, (b) CHBC fine mesh.

Numerical solutions for the three meshes were obtained for final time $t = 8$. The pressure field computed on the finer mesh ($N_{outflow\ \mathrm{bd}} = 24$) is shown in Fig. 14. It can be seen that the incident and scattered acoustic pulse leave the computational domain through the $\Gamma_{outflow\ \mathrm{bd}}$ without the appearance of incoming numerical waves. For each of the three meshes, we computed the $L_2^{E_b}$ error on the boundary elements at the outflow boundary at $t = 8$. The grid converge of the $L_2^{E_b}$ error is presented in Fig. 15. The order of the convergence is 2.97, which is close to the optimal order for the outflow surfaces $m + \frac{1}{2}$ [38] (for our polynomial space is $3 + \frac{1}{2}$).

*4.3.3. The time harmonic source problem*

The last aeroacoustic problem examined is the calculation of the perturbation pressure field generated by a time dependent harmonic source. This problem is a stringent case for the test of the artificial BC because acoustic waves continuously cross the outflow boundary. The time depended acoustic source term has the form

$$S(x,y,t) = \varepsilon \exp\left(-\frac{ln(2)}{w}((x-4)^2 + y^2)\right) sin(\omega t)$$

and is added to the right-hand side of (2.1) for the energy equation. In the numerical experiments we chose $\varepsilon = 0.01$, $w = 1$, $\omega = 0.5\pi$.

The outflow boundary computational domain is

$$\Gamma_{outflow\ bd} = \{(x,y) : x = rcos(\theta), y = rsin(\theta), \quad 0 \leqslant \theta \leqslant 2\pi, r = 10\}.$$

The computational domain is discretized in two triangular meshes, a coarse mesh with 40 elements and a fine mesh with 80 elements on the outflow boundary. As in preivious problems, the local polynomial space is $V_h(E) = \mathbb{P}^3(E)$. Long time integration at final time $t = 350$ was performed. The computed pressure fields on the two meshes are shown in Fig. 16. For both

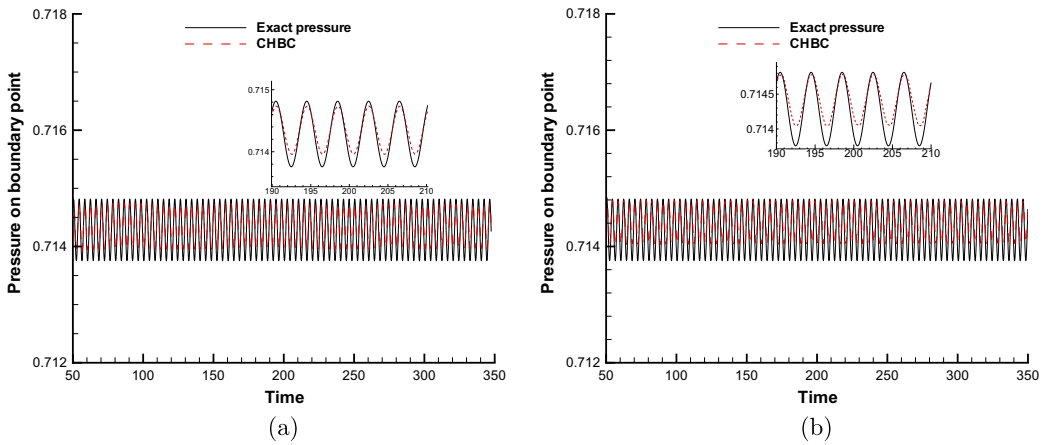


**Fig. 17.** Acoustic time harmonic source problem, $V_h(E) = \mathbb{P}^3(E)$. (a) Coarse mesh. The exact and the numerical boundary point values of the pressure versus time. (b) Fine mesh. The exact and the numerical boundary point values of the pressure versus time.

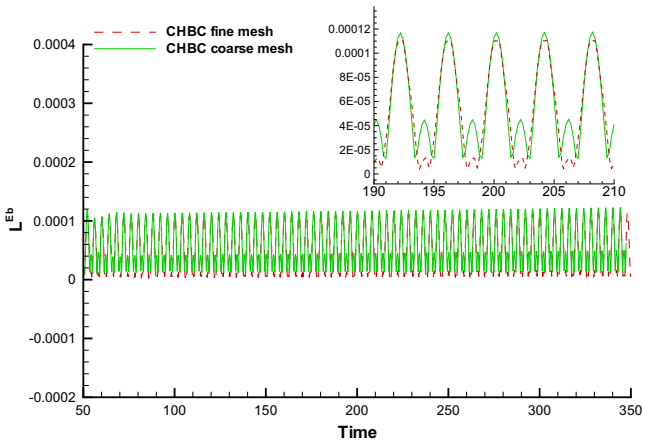


**Fig. 18.** Acoustic time harmonic source problem, $V_h(E) = \mathbb{P}^3(E)$. The time variation of the $L_2^{E_b}$ error for the two meshes.

meshes, the pressure values are recorded at the point $(x,y) = (10,0)$ on the boundary. In Fig. 17(a), point values corresponding to the coarse mesh numerical solution are compared with the exact pressure values. In Fig. 17(b), the same comparison for the point values corresponding to the fine mesh numerical solution is presented. The $L_2^{E_b}$ error is computed on the elements of the boundary for both meshes. In Fig 18, the variations of the $L_2^{E_b}$ error versus time are presented. For both meshes, the $L_2^{E_b}$ error shows periodic variation but remains bounded. Therefore it appears that the proposed characteristic BC approach is accurate and does not deteriorate the stability of the overall numerical scheme.

### 4.4. Viscous flow numerical examples

The proposed characteristic boundary conditions are applied for the numerical solution of compressible viscous flow problems. The Navier–Stokes equations

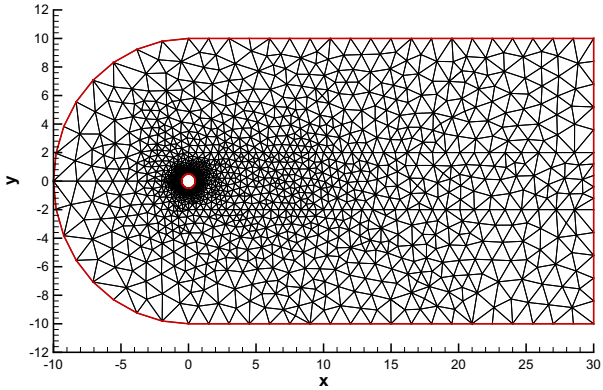


**Fig. 19.** Viscous flow problem, $V_h(E) = \mathbb{P}^3(E)$. The triangulation of the computational domain.

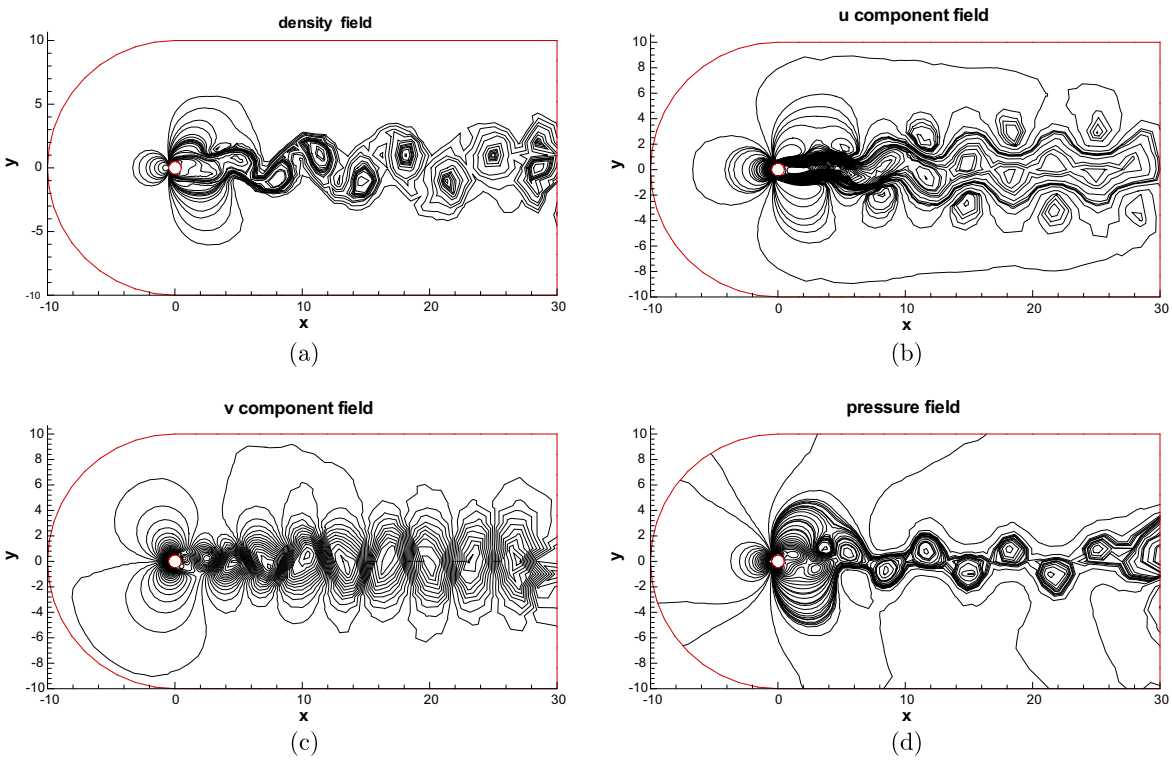


**Fig. 20.** Viscous flow problem, $V_h(E) = \mathbb{P}^3(E)$, the contour plots of the variables at $t = 800$ computed using CHBC. (a) 35 Equally spaced contour lines of the density field, (b) 35 equally spaced contour lines of the $u$ component field, (c) 35 equally spaced contour lines of the $v$ component field, (d) 35 equally spaced contour lines of the pressure field.

$$\partial_t \mathbf{u} + \partial_x \mathbf{f}(\mathbf{u}) + \partial_y \mathbf{g}(\mathbf{u}) - \nabla \cdot (\mathbf{F}_v(\mathbf{u}, \nabla \mathbf{u}), \mathbf{G}_v(\mathbf{u}, \nabla \mathbf{u}) = 0. \tag{4.3}$$

are solved and the viscous fluxes $\nabla \cdot (\mathbf{F}_v(\mathbf{u}, \nabla \mathbf{u}), \mathbf{G}_v(\mathbf{u}, \nabla \mathbf{u}))$ are discretized with $\mathbb{P}^3$ local polynomial space as suggested in [33]. The Navier–Stokes equations due to the presence of viscous fluxes are not a system of pure hyperbolic type equations. In addition, the viscous fluxes can not be expressed as functions of the characteristic waves, e.g. in flux form similar to (3.7). Viscous effects for the inflow/outflow boundaries are negligible, therefore the BC's developed for the Euler equations can be used. The CHS, on the $E_m$ has the same form as in (3.9) (we do not add any viscous term as source on the right hand-side of CHS form).

Viscous subsonic flow over a cylinder at Reynolds number $Re = 200$ is computed. The computational domain $\Omega$ with its triangulation is shown in Fig. 19. The cylinder surface is discretized by 42 elements and the total number of the elements is $N_{el} = 2729$. The outflow boundary is comprised by the curves

$$\Gamma_{outblow\ bd} = \{(x, y) : 0 \leqslant x \leqslant 30, y = \pm 10\} \bigcup \{(x, y) : x = 30, -10 \leqslant y \leqslant 10\}.$$

The problem is solved numerically at final time $t = 800$. The computed flow field for the primitive variables is presented in Fig. 20 where: (a) for density $\rho$, 35 equally distributed contours between $\rho_m = 0.901$ to $\rho_M = 1.030$ have been used, (b) for the $u$ velocity component, 35 equally distributed contours between $u_m = -0.018$ to $u_M = 0.355$ have been used (c) for the $v$ velocity component, 35 equally distributed contours between $v_m = -0.169$ to $v_M = 0.174$ have been used and (d) for the pressure $p$, 35 equally distributed contours between $p_m = 0.67$ to $p_M = 0.74$ have been used. The values of each of the primitive variables at the boundary point $N_{bd} = (30, 0)$ have been recorded. The variations of these values in time are shown in Fig. 21. It can be seen that the variation of the values for all variables is periodic in time and both the amplitude and the period are constant. Fig. 21 shows that the reflected waves are weak and do not influence the periodic behavior of the solution even for long time integration. The same problem was solved on an enlarge domain, similar to the domain of Fig. 19, but extended 10 diameters more in all directions. Simple extrapolated boundary conditions (ExtrBC) were used on the outflow boundary. In Fig. 22 the variation of the variables for the same point $N_{bd} = (30, 0)$, as in Fig. 21 is shown. The variations shown in Fig. 22, however, correspond to an interior point and it appears that extrapolation BC significantly affects the solution and precludes periodic evolution.

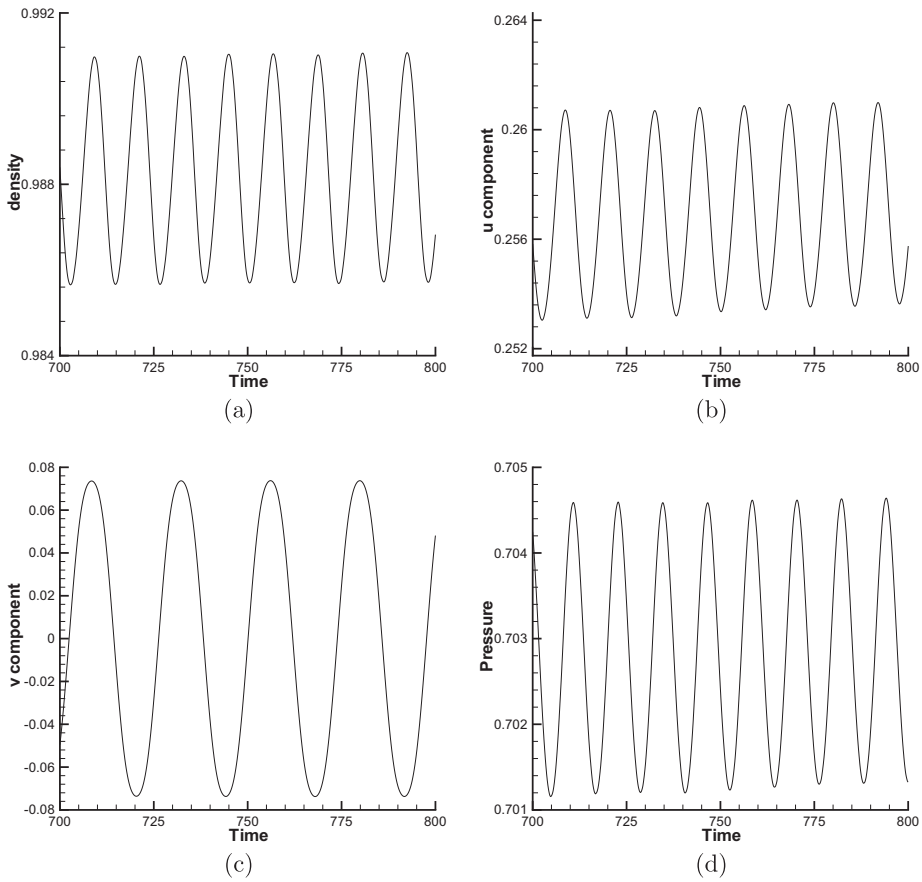


**Fig. 21.** Viscous flow problem, $V_h(E) = \mathbb{P}^3(E)$, point values computed using CHBC. (a) Density values on point $N_{bd} = (30, 0)$ versus time. (b) $u$ Values on point $N_{bd} = (30, 0)$ versus time. (c) $v$ Values on point $N_{bd} = (30, 0)$ versus time. (d) Pressure values on point $N_{bd} = (30, 0)$ versus time.

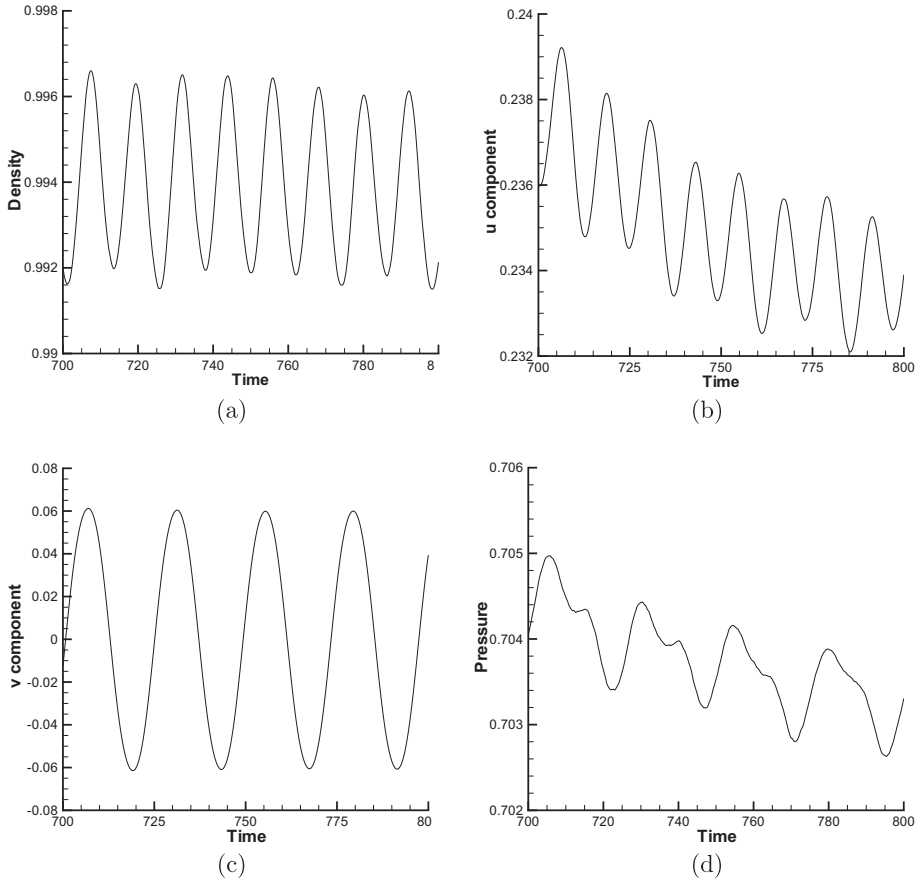


**Fig. 22.** Viscous flow problem, the variation of the point values for the expanded domain using ExtrBC. (a) Density values on point $N_{bd} = (30,0)$ versus time. (b) $u$ Values on point $N_{bd} = (30,0)$ versus time. (c) $v$ Values on point $N_{bd} = (30,0)$ versus time. (d) Pressure values on point $N_{bd} = (30,0)$ versus time.

## 5. Conclusions

Artificial boundary conditions based on the characteristic analysis of the Euler's equations were developed and applied in the DG framework. The present formulation can be extended to three dimensions and it is applicable to boundaries of arbitrary shape. An auxiliary system was constructed through application of characteristic analysis. The numerical solution of this system is used for the evaluation of the time variation of the characteristic waves which cross the artificial boundary. The time variation of these waves was related to the conservative variables time variation resulting in an ODE system. The numerical solution of this system mimics adequately the analytical boundary data. Computed results with the proposed boundary conditions demonstrated that complex flow features can be convected outside the computational domain with little distortion. In addition, propagation of small amplitude acoustic-type perturbations with the proposed boundary conditions demonstrated equally good performance with exact boundary data. Application of the proposed artificial BC performed well for the computation of viscous flow past a cylinder and demonstrated superior performance compared to simple extrapolation boundary data specification.

## Acknowledgements

This effort was sponsored by the Air Force Office of Scientific Research, Air Force Material Command, US Air Force, under Grant FA 86550713099.

## Appendix A. The artificial boundary conditions for the linearized Euler equations

The two dimensional linearized Euler equations have the form

$$\partial_t \mathbf{u} + A\mathbf{u}_x + B\mathbf{u}_y = 0, \tag{A.1}$$

with

$$\mathbf{u} = \begin{bmatrix} u \\ v \\ p \end{bmatrix}, A = \begin{bmatrix} M_x & 0 & 1 \\ 0 & M_x & 0 \\ 1 & 0 & M_x \end{bmatrix}, B = \begin{bmatrix} M_y & 0 & 0 \\ 0 & M_y & 1 \\ 0 & 1 & M_y \end{bmatrix}$$

where $\mathbf{u}$ is the solution variable vector with components the velocity $\mathbf{v} = (u, v)$ and $p$ is the pressure. $A$, $B$ are constant coefficient matrices where $M_\infty = (M_x, M_y)$ is the free stream speed. We apply our analysis in direction $\mathbf{n} = (1, 0)$. The matrix $A$ is written in the form $A = R\Lambda R^{-1}$. Multiplying the system (A.1) by $R^{-1}$ obtain

$$\frac{\partial \mathbf{w}}{\partial t} + \Lambda \frac{\partial \mathbf{w}}{\partial x} + B_w \frac{\partial \mathbf{w}}{\partial y} = 0, \tag{A.3}$$

where $\mathbf{w}$ and $\Lambda$, $B_w$ are

$$R^{-1}\mathbf{u} = \mathbf{w} = \begin{pmatrix} w_1 \\ w_2 \\ w_3 \end{pmatrix} = \begin{pmatrix} u + p \\ \sqrt{2}v \\ u - p \end{pmatrix}. \tag{A.4}$$

$$\Lambda = diag(\lambda_1, \lambda_2, \lambda_3) = diag(M_x + 1, M_x, M_x - 1),$$

$$B_w = R^{-1}B = \begin{pmatrix} M_y & \frac{1}{\sqrt{2}} & 0 \\ \frac{\sqrt{2}}{2} & M_y & -\frac{\sqrt{2}}{2} \\ 0 & -\frac{\sqrt{2}}{2} & M_y \end{pmatrix}. \tag{A.5}$$

The system (A.3) is equivalent with the system (A.1), but in general this is not true for the systems (3.8) and (3.1). Omitting the term $B_w \frac{\partial \mathbf{w}}{\partial y}$ from (A.3), we get the CHS for the linearized Euler equations

$$\frac{\partial \mathbf{w}}{\partial t} + \Lambda \frac{\partial \mathbf{w}}{\partial x} = 0. \tag{A.6}$$

System (A.6) expressed in $\mathbf{u}$ variables is solved numerically using DG discretization as before (see (3.9) and (3.13)). The procedure applied here deals with the procedure followed in [39] (see also [10,40–42]), where suitable boundary conditions are considered for the problem (A.1) in order to achieve solution uniqueness.

## References


[1] D. Givoli, Non-reflecting boundary conditions, J. Comput. Phys. 91 (1991) 1–29.
[2] T. Colonious, Modeling artificial boundary conditions for compressible flow, Ann. Rev. Fluid 36 (2004) 315–345.
[3] D.J. Bodony, Analysis of sponge zones for computational fluid mechanics, J. Comput. Phys. 212 (2005) 681–702.
[4] D. Appelo, T. Colonius, A high-order super-grid-scale absorbing layer and its application to linear hyperbolic systems, J. Comput. Phys. 228 (2009) 4200–4217.
[5] T. Colonius, H. Ran, A super-grid-scale model for simulating compressible flow on unbounded domains, J. Comput. Phys. 182 (2002) 191–212.
[6] P. Balakumar, H. Zhao, H. Atkins, Stability of hypersonic boundary layer over a compression corner, in: AIAA Paper 2002-2848, 2002.
[7] S. Pirozzoli, F. Grasso, T. Gatski, Direct numerical simulation and analysis of a spatially evolving supersonic turbulent boundary layer at $m = 2.25$, Phys. Fluids 16 (2004) 530–545.
[8] B. Gustafsson, H. Kreiss, Stability theory of difference approximations of mixed initial boundary value problems, Math. Comput. 26 (1972) 649–686.
[9] F.Q. Hu, X.D. Li, D.K. Lin, Absorbing boundary conditions for nonlinear Euler and Navier Stokes equations based on the perfectly matched layer technique, J. Comput. Phys. 227 (2008) 4398–4424.
[10] D. Kröner, Absorbing boundary conditions for the linearized Euler equations in 2D, Math. Comput. 57 (1991) 153–167.
[11] K.W. Thompson, Time dependent boundary conditions for hyperbolic systems, J. Comput. Phys. 68 (1987) 1–24.
[12] M. Giles, Nonreflecting boundary conditions for euler calculations, AIAA J. 28 (1990) 2050–2058.
[13] C.K. Tam, J.C. Webb, Dispersion–relation-preserving finite difference schemes for computational acoustics, J. Comput. Phys. 107 (1993) 262–281.
[14] T. Hagstorm, Radiation boundary conditions for the numerical simulation of wavers, Acta Numer. 8 (1999) 47–106.
[15] R. Hixon, S.H. Shih, R.R. Mankbadi, Evaluation of boundary conditions for computational aeroacoustics, AIAA J. 33 (1995) 2006–2012.
[16] Y. Zhou, Z. Wang, Absorbing boundary conditions for the Euler and Navier–Stokes equations with the spectral difference method, J. Comput. Phys. 229 (2010) 8733–8749.
[17] K.W. Thompson, Time-dependent boundary conditions for hyperbolic systems. II, J. Comput. Phys. 89 (1990) 439–461.
[18] T. Poinsot, S. Lele, Boundary conditions for direct simulations of compressible viscous flows, J. Comput. Phys. 101 (1992) 104–129.
[19] L. Selle, F. Nicoud, T. Poinsot, Actual impedance of nonreflective boundary conditions: implications for computation of resonators, AIAA J. 42 (2004) 958–964.
[20] T. Colonious, S.K. Lele, P. Moin, Boundary conditions for direct computation of aerodynamic sound generation, AIAA J. 31 (1993) 1574–1582.
[21] T. Colonious, Numerical nonreflecting boundary and interface conditions for compressible flow and aeroacoustic computations, AIAA J. 35 (1997). 1113-1126.
[22] X. Chen, G. Zha, Implicit application of non-reflective boundary conditions for Navier–Stokes equations in generalized coordinates, AIAA paper, 2005, 2005-0091.
[23] I. Toulopoulos, J.A. Ekaterinaris, High-order discontinuous-Galerkin discretizations for computational aeroacoustics in complex domains, AIAA J. 44 (2006) 502–511.
[24] J. Qiu, B.C. Khoo, C.W. Shu, A numerical study for the performance of the Runge–Kutta discontinuous Galerkin method based on different numerical fluxes, J. Comput. Phys. 212 (2006) 540–565.
[25] B. Cockburn, C. Shu, The Runge–Kutta discontinuous Galerkin method for conservation laws, multidimensional systems, J. Comput. Phys. 141 (1998) 199–224.
[26] G.W. Hedstrom, Nonreflective boundary conditions for the nonlinear hyperbolic systems, J. Comput. Phys. 30 (1979) 222–237.

[27] C. Hirsch, Numerical Computation of Internal and External Flows, Computational Methods for Inviscid and Viscous Flows of Wiley Series in Numerical Methods in Engineering, vol. 2, Wiley, 1988.
[28] P. Lesaint, P.A. Raviart, On a finite element method for solving the neutron transport equation, in: C. de Boor (Ed.), Mathematical Aspects of Finite Element in Partial Differential Equations, Academic Press, New York, 1974, pp. 89–123.
[29] C. Johnson, J. Pitkaranta, An analysis of the discontinuous Galerkin method for scalar hyperbolic equation, Math. Comp. 46 (1986) 1–26.
[30] C. Johnson, Numerical Solutions of Partial Differential Equations by the Finite Element Method, Cambridge University Press, 1987.
[31] J. Nordström, Accurate solutions of the Navier–Stokes equations despite unknown outflow boundary data, J. Comput. Phys. 120 (1995) 184–205.
[32] M. Svärd, M.H. Carpenter, J. Nordström, A stable high-order finite difference scheme for the compressible Navier–Stokes equations far-field boundary conditions, J. Comput. Phys. 225 (2007) 1020–1038.
[33] F. Bassi, S. Rebay, A high-order accurate discontinuous finite element method for the numerical solution of the compressible Navier–Stokes equations, J. Comput. Phys. 131 (1997) 267–279.
[34] J. Hardin, J. Ristorcelli, C.K. Tam, Icase/larc workshop on benchmark problems in computational aeroacoustics (caa), nasa cp 3300, 1995.
[35] A. Verhoff, Far-field computational boundary conditions for two-dimensional external flow problems, AIAA J. 30 (1992) 2585–2594.
[36] A. Verhoff, Global far-field computational boundary conditions for C- and O-grid topologies, AIAA J. 36 (1998) 148–156.
[37] J. Nordström, On extrapolation procedures at artificial outflow boundaries for the time-depentet Navier–Stokes equations, Appl. Numer. Math. 23 (1997) 457–468.
[38] P. Monk, G.R. Richter, A Discontinuous Galerkin method for linear symetric hyperbolic systems in inhomogeneous media, J. Sci. Comput. 22–23 (2005) 443–477.
[39] R.L. Higdon, Initial-boundary value problems for linear hyperbolic systems, SIAM Rev. 28 (1986) 177–217.
[40] E.C. Zachmanoglou, Introduction to Partial Differential Equations with Applications, Williams and Wilkins Company (1976).
[41] I. Toulopoulos, Numerical Solutions of Hyperbolic Systems by Discontinous Galerkin Finite Element Method, Ph.D. Thesis, Department of Mathematics University of Athens, 2009 (in Greek).
[42] K. Adamy, Contribution a l'etude theorique et numerique de cer- tains systems de mecanique des fuides, Ph.D. Thesis, These de doctorat de l'université Paris XI, 2008.